TECHNISCHE UNIVERSITÄT MÜNCHEN
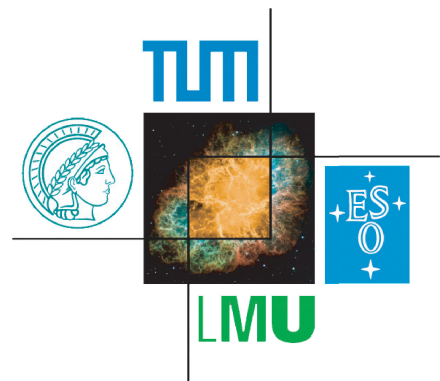
Physik-Department E12 - Dense and strange hadronic matter
Excellence Cluster - 'Origin of the Universe'

Development of a self-triggered detector system for the detection of secondary pion beams

MASTER THESIS

Joana Katharina Wirth

June 23, 2015

Zusammenfassung

Im Jahr 2014 führte die HADES Kolloboration zwei erfolgreiche Experimente mit sekundären Pionenstrahlen durch. Da sekundäre Pionenstrahlen stark in Position und Impuls defokussiert sind und nur durch die Akzeptanz der Strahlführungselemente ($\Delta p/p \approx 8\,\%$) limitiert werden, wurden zwei schnelle Spurenrekonstruktionsstationen (CERBEROS: Central Beam Tracker for Pions) entwickelt und anschließend entlang der Pionenstrahl-Schikane nach dem Pionen-Produktionstarget installiert, um den Impuls jedes einzelnen Pions zu messen. Der Impuls wird auf der Basis der Positionsinformation jedes Treffers (Hits), der von den beiden Stationen detektiert wird, und der Berechnung basierend auf den Strahlführungselementen rekonstruiert. Um der Anforderung der später durchgeführten exklusiven Analyse der untersuchten Reaktionen gerecht zu werden, ist es unverzichtbar den Impuls mit einer Auflösung besser als $0.5\,\%$ zu messen.

Im Verlauf der vorliegenden Arbeit wird das Konzept von CERBEROS beschrieben. Beide Messstationen bestehen aus einem doppelseitigen Siliziumstreifenzähler mit einer großen aktiven Fläche ($10 \times 10\,\mathrm{cm}^2$), der in einer Vakuumkammer ($10^{-7}\,\mathrm{mbar}$) angebracht wurde, die passend auf das Strahlrohr montiert ist. Um die schnelle Spurenrekonstruktion zu gewährleisten, werden die Sensoren mit dem n-XYTER ASIC Chip ausgelesen. Aufgrund seiner selbsttriggernden Architektur und internen Speicherfähigkeit, erlaubt der Chip simultane Beobachtungen bei hohen Raten ($dN/dt > 10^6$ part./s). Das TRB3-Ausleseboard, auf dem die Triggerlogik implementiert ist, integriert das System in die bestehende HADES Datenaufnahme.

Die Analyse der während der beiden Strahlzeiten aufgenommenen Daten wird mit besonderem Schwerpunkt auf der Hitrekonstruktion der x- und y-Positionen und der Impulsrekonstruktion basierend auf der Hitposition in beiden Stationen durchgeführt. Zuvor wurde eine Impulskalibrierung mit einem monochromatischen Protonenstrahl bei sechs verschiedenen Impulsen in Relation zu dem Zentralimpuls von $2.68\,\mathrm{GeV/c}$ ausgeführt. Durch diese Kalibrierung wurden die rekonstruierten Impulse mit dem Referenzwert in Übereinstimmung gebracht. Auch die Auflösungen der rekonstruierten Werte liegt im Rahmen der Anforderung ($0.5\,\%$) variierend zwischen $18\,\%$-$29\,\%$. Eine systematische Untersuchung der breiten Impulsverteilung des sekundären Pionstrahls wurde bei fünf verschiedenen Zentralimpulsen zwischen $0.656\,\mathrm{GeV/c} < p_{\pi^-} < 1.7\,\mathrm{GeV/c}$ durchgeführt. Verschiedene Auswahlmethoden der Pionen mit einem bestimmten Impuls, die mit dem Target interagiert haben, wurden untersucht. In diesem Zusammenhang wurde außerdem der rekonstruierte Impuls mit den Events aus der elastischen Streuung ($\pi^- + p$) verglichen, die während der zweiten experimentellen Kampagne ($0.656\,\mathrm{GeV/c} < p_{\pi^-} < 0.800\,\mathrm{GeV/c}$) aufgenommen wurden. Im Zuge dessen wurde auch der Vergleich zwischen der $\sqrt{s}$ Verteilung, die mit dem rekonstruierten Impuls berechnt wurde, mit der invarianten Masseverteilung des $\pi^- p$-Systems gezogen. Aufgrund der Verschiebung der invarianten Masseverteilung zu kleineren Werten verglichen mit der $\sqrt{s}$ Verteilung, wurde eine erste Abschätzung des Energieverlusts der Pionen und Protonen im Target basierend auf einer GEANT4 Simulation durchgeführt. Insgesamt hat CERBEROS eine exzellente Performance mit der Impulsrekonstruktionseffizienz von $78.4\,\%$ bei $0.690\,\mathrm{GeV/c}$ und sogar $87\,\%$ bei $1.7\,\mathrm{GeV/c}$ demonstriert.

Abstract

In 2014 the HADES collaboration performed two successful physics production runs with secondary pion beams. Since secondary pion beams are strongly defocussed in position and momentum only limited by the beamline acceptance ($\Delta p/p \approx 8\,\%$ at SIS18, GSI), two fast tracking stations (CERBEROS: Central Beam Tracker for Pions) were developed and finally installed along the pion beam chicane following the pion production target providing the momentum measurement of each individual pion. The momentum is reconstructed on the basis of the position information of every hit detected by the tracking stations and the beam optics transport calculation. To meet the demand of the exclusive analysis for some reaction channels it is mandatory to measure the momentum with a resolution below $0.5\,\%$.

In this thesis the concept developed for CERBEROS is described. Both tracking stations consist of a double-sided silicon strip sensor with a large active area ($10 \times 10\,\mathrm{cm}^2$) placed in a vacuum chamber compatible to the beam pipe mechanics (10^{-7} mbar). To guarantee fast tracking, the sensors are read out with the n-XYTER ASIC chip. Due to its self-triggering architecture and local storage capability, the chip enables on-line monitoring at high rates ($\mathrm{dN/dt} > 10^6$ part./s). The TRB3 on which the trigger logic is implemented integrates the system into the HADES DAQ.

Moreover, the analysis of the data obtained during both pion-induced experimental campaigns is presented with special emphasis on the hit reconstruction of the x- and y-positions of each sensor as well as the momentum reconstruction based on the hit information of both tracking stations. Furthermore, the momentum calibration performed prior with a monochromatic proton beam at six different known momenta with respect to the central beam momentum of $2.68\,\mathrm{GeV/c}$ is addressed. Throughout this calibration procedure all reconstructed momenta were in good agreement with the reference values with resolutions below the requirement ($0.5\,\%$) varying between $18\,\% \leq \sigma \leq 29\,\%$. Concerning the broad momentum distribution of the non-monochromatic secondary pion beam, a systematic study at the five central beam momenta varying from $0.656\,\mathrm{GeV/c} < p_{\pi^-} < 1.7\,\mathrm{GeV/c}$ was carried out. Several selection methods of the pion with a certain momentum that finally interacted with the target were investigated including a comparison of the reconstructed pion momentum with the elastic scattering events ($\pi^- + p$) recorded during the second experimental campaign ($0.656\,\mathrm{GeV/c} < p_{\pi^-} < 0.800\,\mathrm{GeV/c}$). In the same context the $\sqrt{s}$ distribution calculated with the reconstructed pion momentum was compared to the invariant mass spectrum of the $\pi^- p$-system reconstructed within the HADES spectrometer. Due to a shift of the invariant mass spectrum to lower values compared to the $\sqrt{s}$ distribution, a first estimation of the energy loss of the pions and protons in the target based on a GEANT4 simulation was carried out. All in all CERBEROS demonstrated an excellent performance with momentum reconstruction efficiency of $78.4\,\%$ at $0.690\,\mathrm{GeV/c}$ and even $87\,\%$ at $1.7\,\mathrm{GeV/c}$.

Contents

1 Introduction

In the past the HADES collaboration performed several experimental campaigns with proton and heavy ion beam, whereas the existing measurements were recently completed with a secondary pion beams. During the experimental campaigns elementary reactions $(\pi^- + p)$ at several momenta varying from $0.656\,\mathrm{GeV/c} < p_{\pi^-} < 0.800\,\mathrm{GeV/c}$ as well as pion-nucleus reactions $(\pi^- + A$, with A=C or A=W) at $p_{\pi^-} = 1.7\,\mathrm{GeV/c}$ have been measured.

1.1 Physics motivation for pion-induced reactions

In the strangeness sector pion-induced reactions are of special interest to enrich the existing data set, that is rather old and with poor statistic. It offers the possibility to investigate the production of strangeness and to compare it with photon- and proton-induced reactions, that have already been studied in several experiments. All the three different production mechanisms are illustrated in Fig. 1.1. In photon-induced reactions the strangeness production occurs all over the whole volume $(\sigma \sim A)$. In case of the proton-induced reactions strangeness is produced close to the surface $(\sigma \sim A^{0.8})$ with an additional creation of secondary pions, whereas in pion-induced reactions the production happens mainly on the surface $(\sigma \sim A^{2/3})$. Thus, the particle production mechanisms are easier to model. The main focus during the first secondary pion beam campaign with the HADES spectrometer was on the investigation of strangeness production as well as the properties of K_S^0, K^+, Φ and K^- in cold nuclear matter $(\pi^- + A)$.
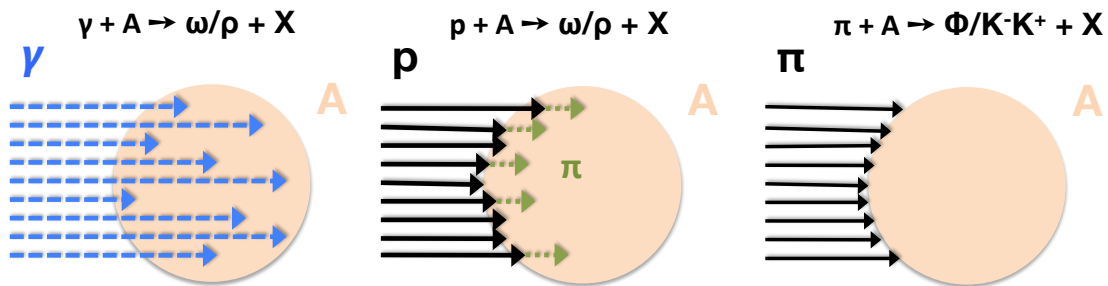

Figure 1.1: Strangeness production mechanism for photon-, proton- and pion-induced reactions.

For the K^+ and K^0 no conventional absorption mechanism exits. However, K^- mesons can be absorbed in nuclear environment through strangeness exchange processes $(K^- N \to Y\pi$, $K^- NN \to YN)$ or resonance excitation. The K^0 production in pion-induced reactions was already studied by the FOPI collaboration for several nuclei. There the cross section (Fig. 1.2 (a)) was extracted to scale with the surface of the nucleus: A^b, $b = 2/3$. One question that can be addressed now is how the K^- yield behaves? According to the theoretical prediction the kaon mass is increased and the antikaon mass decreased because of the repulsive and attractive

interaction of the two particle species with nuclear matter. Thereby, a drop of the effective mass (Fig. 1.2 (b)) and thus a decrease of the kinematical threshold would lead to $b > 2/3$. However, if an increase of the absorption with A would be dominant, one should observe a $b < 2/3$.
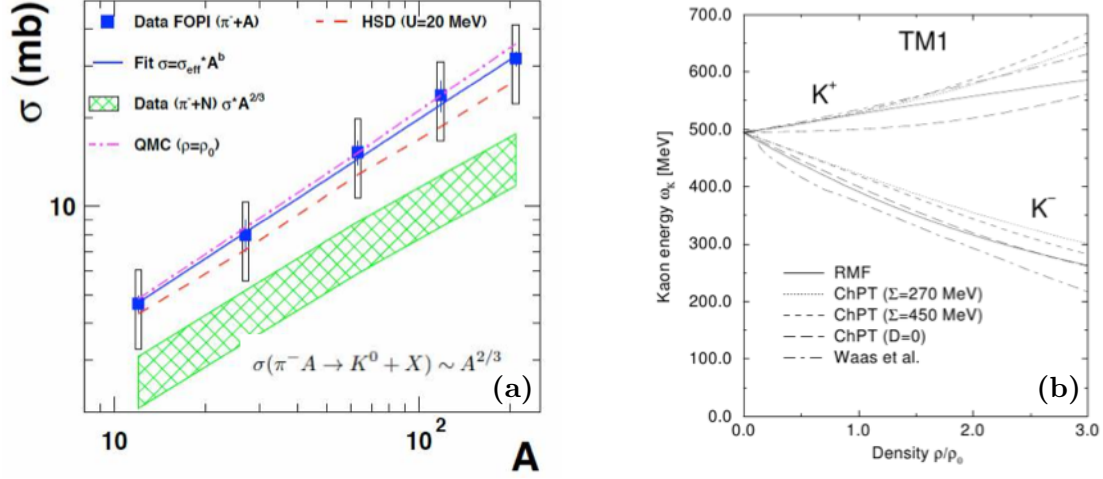

Figure 1.2: **(a)** Cross section σ of the K^0 inclusive production as a function of the mass number A of the target nuclei (squares) fitted with a power law function (solid line). [Ben09] **(b)** The K^+ and K^- effective energy (mass) in nuclear matter as a function of baryon density. [Sch97]
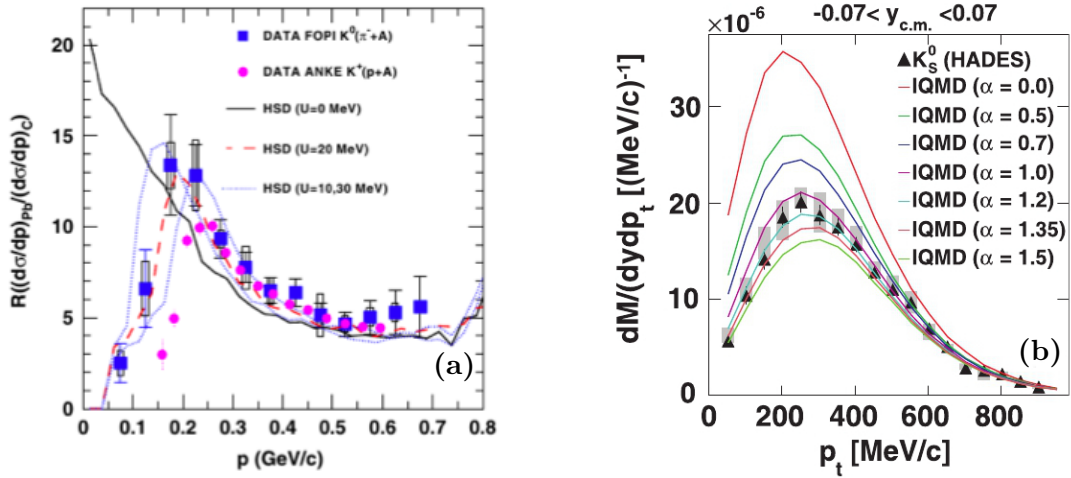

Figure 1.3: **(a)** Ratio of the K^0 (K^+) yield produced by pions (protons) on heavy and light targets as a function of momentum p in the lab system. The yield ratio of K_S^0 produced by pions impacting on Pb and C targets (blue squares) as well as the yield ratio of K^+ in proton-induced reactions on Au and C targets (full circles). The different strengths of the KN potential included in the HSD model are depicted in solid (black), dashed (red) and dotted (blue) lines. [Ben09]**(b)** The p_T distribution of the K_S^0 at mid-rapidity (full symbols) compared with the IQMD model, whereby the different solid lines correspond to variations of the parameter α, which couples directly to the potential strength. [Aga10]

In terms of the properties of K^0 and K^+ in cold nuclear matter, the real part of the interacting potential between kaons (K^0,K^+) and nucleons can be further analysed. For the existing data sets

where the K^0-nucleon potential was extracted by comparing the ratio of the momentum distributions obtained with $\pi^- + Pb$ to $\pi^- + C$ by the FOPI collaboration (Fig. 1.3 (a)), the potential was found to be repulsive leading to a depletion in the low momentum region. Pion-induced reactions open up the possibility to measure the low p_T region, which is especially sensitive to the repulsive potential and complete the studies of the K^0 properties in $Ar + KCl$ (Fig. 1.3 (b)), $p + p$ and $p + Nb$ by the HADES collaboration [Aga14b] [Aga14a]. Moreover, it can give further evidence on the strength of the repulsive potential, since the FOPI collaboration extracted a value of about $20\,\mathrm{MeV}$ contrary to the one obtained by the HADES collaboration with a value of around $40\,\mathrm{MeV}$ [Ben09] [Aga10].

The second physics production run with pion beams was devoted to the study of the production of baryonic resonances and vector mesons in elementary reactions ($\pi^- + p$). Although an extended data statistic is existing for γ-induced reactions, pion-induced reactions have not been investigated to the same extend yet. Compared to ultra-relativistic heavy-ion reactions where the initial state of the nuclear medium is far from equilibrium, the $\pi^- + p$ reactions allows to pin down the vacuum properties of the different baryonic resonances and their coupling to the different final states. These measurements are mandatory reference to interpret the spectra measured in $\pi^-, p + A$ and heavy ion collisions. [Eff99]
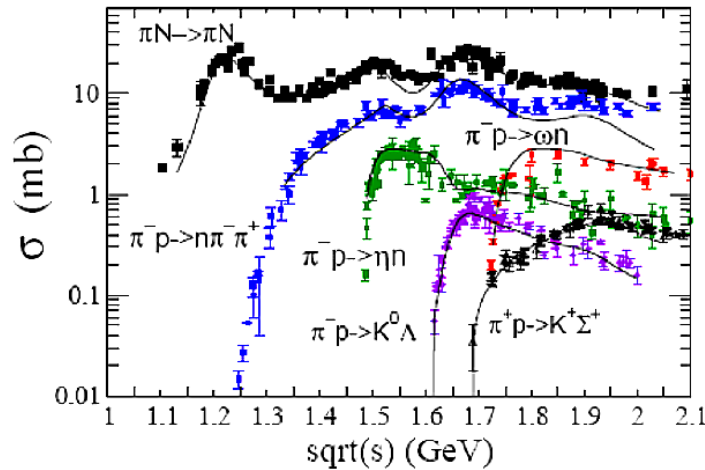

Figure 1.4: Cross section as a function of $\sqrt{s}$ for pion-induced reactions based on the existing world data whereas the black line indicates the coupled-channel Giessen model. [Sh08]

For the study of baryonic resonances, $\pi + N$ collisions offer a fixed $\sqrt{s_{\pi N}}$ corresponding to a fixed resonance mass allowing for an easier distinction of the contributions from different resonances, whereas in $A + A$ and $p + p$ the excitations of resonances takes place at various energies. The double-pion production ($\pi^- p \rightarrow n\pi^+\pi^-$) is of particular interest, since it has the largest yield among the inelastic channels (Fig. 1.4) with a large resonance contribution. Today's knowledge about the N^* coupling to ρN, $\pi\sigma$ and σN channel in πN reactions (Fig. 1.5) is based on bubble chamber experiments by Manley, Arndt, Goradia, Teplitz [Man84]. The disentangling of the different resonance contributions and therefore the branching ratios of the coupling to vector mesons achieved with higher statistics can deliver further constraints for the Partial Wave Analyses (PWA) and offers the possibility to perform a combined PWA of pion- and photon-induced reactions. [Wei] [Fab13]
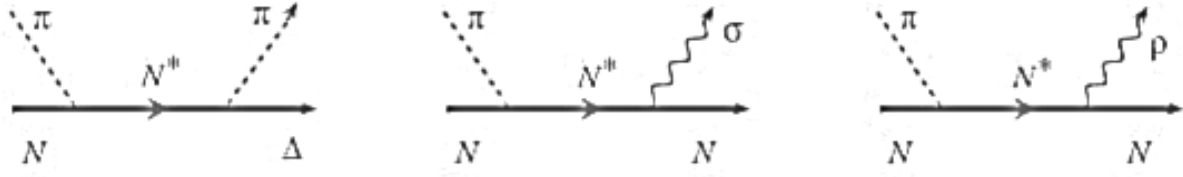
Figure 1.5: Schematic of the N^* coupling to the ρN, $\pi \Sigma$ and σN channel in πN reactions.

Furthermore, the study of the baryonic resonance (N^*) coupling to off-shell vector mesons in $\pi^- p \to n e^+ e^-$ reactions below the ω threshold is of great interest. Especially the the origin of in-medium modifications of the vector mesons' spectral functions is assumed to be driven by these couplings. The contribution of the baryonic resonances in the dilepton spectrum can be explained either by the decay of these resonances into ρ and ω, that subsequently decay into $e^+ e^-$ or by the Dalitz decay ($N^* \to n e^+ e^-$) together with the time-like electromagnetic form factor including the electromagnetic structure of this baryonic transition (Fig. 1.6). During the HADES pion beam campaign $\pi^- + p$ reactions with $\sqrt{s}$ varying from 1.468 GeV to 1.556 GeV have been measured, covering the region of the pole mass of the resonance $N^*(1520)$, which is believed to have a strong coupling to the ρ meson. Besides, the $N^*(1440)$ and $N^*(1535)$ have a huge contribution in this energy region. Thereby, the investigation of the spectral destructive interference between the iso-scalar (off-shell ω) and the iso-vector (off-shell ρ) is of special interest and has been predicted to occur with a maximum effect at $\sqrt{s} = 1.55$ GeV, so at $p_{\pi^-} = 0.8$ GeV/c, with an almost total cancellation. [Wei] [Fab13]
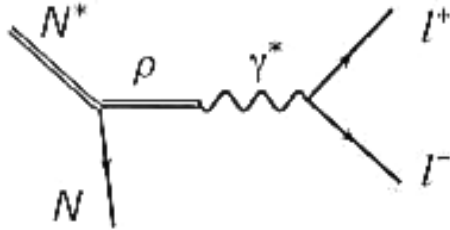

Figure 1.6: Nucleon resonance production with subsequent Dalitz decay.

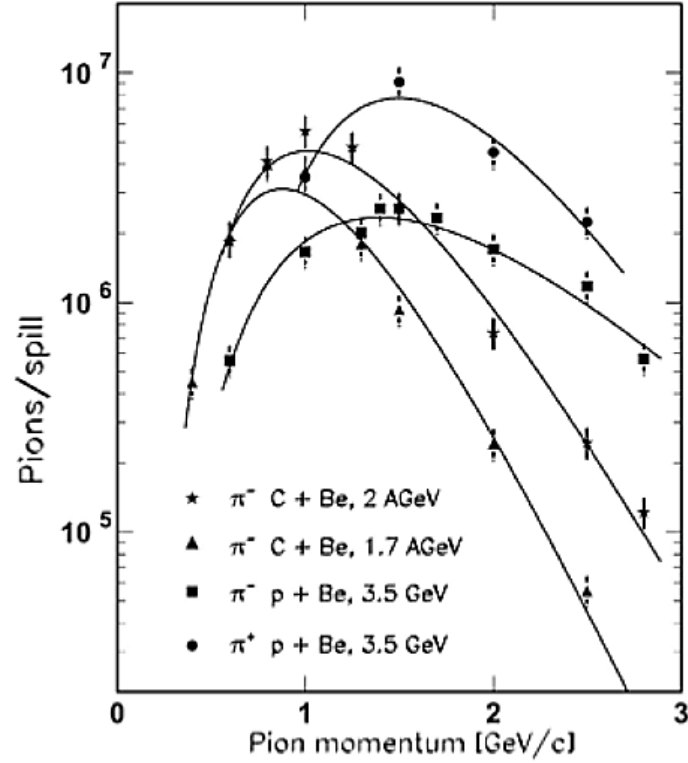## 1.2 CERBEROS: Central Beam Tracker for Pions

Figure 1.7: Pions per spill at the HADES target for different primary beams (p and C) as a function of central beam momentum of the pion beam chicane. The numbers are extrapolated in terms of the maximum intensity restricted by the space-charge limit of the SIS18 [Dia02].

Secondary pion beams are created at GSI by impinging high intensity primary proton or ion beams ($dN/dt \sim 10^{11}$ part./s) on a Beryllium target at the GSI. The $18.4\,g/cm^2$ dense production target has a length of $10\,cm$ with a pencil shape along the first $3\,cm$ with a diameter of $7\,cm$ tapering to a final diameter of $4\,cm$. A primary ion beam with 2 AGeV is employed leading to a maximum spill at the HADES target (Fig. 1.7) covering the range of the central beam momentum from $0.656\,GeV/c$ to $1.7\,GeV/c$. Due to technical reasons the primary Carbon beam was replaced by a primary Nitrogen beam. Both are comparable considering that the energy per nucleon is equal. [Dia02] [Spr08]

During the collision different particle species are produced including positively and negatively charged pions. Since the proton contamination is quite huge when selecting π^+, negatively charged particles including π^- are chosen by the beamline settings. Afterwards the π^- are transported along the pion beam chicane to the HADES spectrometer, depicted in Fig. 1.8. Since the pions have a huge spread in both, momentum and angle, only limited by the beamline acceptance ($\Delta p/p \approx 8\,\%$), two fast tracking stations that provide a momentum measurement of each individual pion with a resolution below $0.5\,\%$ have been developed. The momentum is evaluated using the beam optics transport code and the position information of each hit detected by the double sided silicon sensor located along the pion beam chicane at two different positions indicated in green in Fig. 1.8. The tracking stations play an important role for the exclusive analysis of investigated reactions like $\pi^- + p \rightarrow n e^+ e^-$ concerning the contributions of the different baryonic resonances

(Section 1.1), which is especially challenging with respect to minimum ionizing particle detection and on-line monitoring of high beam rates (dN/dt $> 10^6$ part./s). [Dia02]

To guarantee fast tracking, a silicon sensors readout with the n-XYTER chip has been employed. Due to its self-triggering architecture and local storage capability, the n-XYTER enables on-line tracking of each individual pion. Moreover, it provides time information which enables the possibility to correlate the events in the first and second detector. The readout chain is completed by the TRB3, allowing the integration of the secondary beam tracker into the HADES data acquisition system and the operation as a stand alone system.
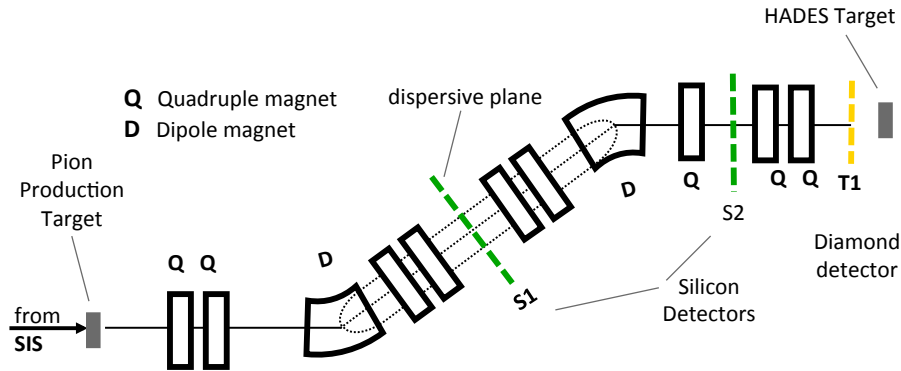
Figure 1.8: Schematic of the pion beam chicane. A primary Nitrogen beam is impacting on a pion production target (Beryllium target). The thereby produced pions are transported along the beam line to the HADES spectrometer. Indicated in green is the position of the silicon stations. The first one is located at the dispersion plane.

2 The HADES experiment
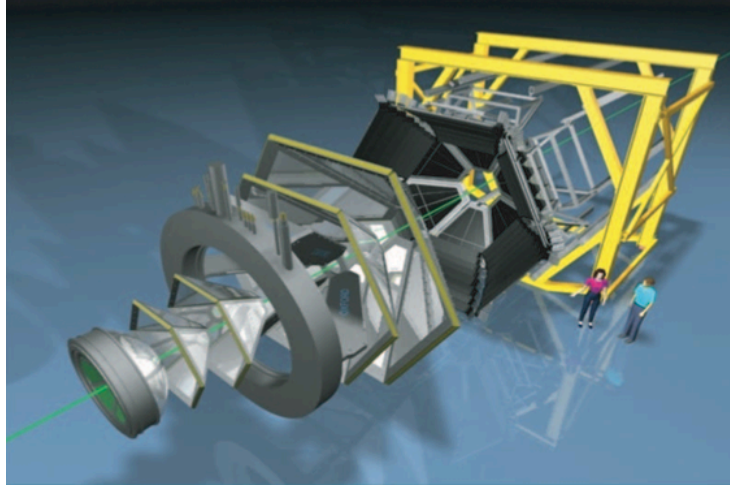
Figure 2.1: Expanded view of the HADES detector system, where the green line indicates the particle beam.

The **H**igh **A**cceptance **D**i-**E**lectron **S**pectrometer (HADES) (Fig. 2.1) is a fixed target experiment located at the SIS18 [1] of the GSI Helmoltzzentrum für Schwerionenforschung GmbH in Darmstadt (Germany). The SIS18 with a magnetic rigidity of 18mT, can deliver protons with a maximum kinetic energy of $4.5\,\mathrm{GeV}$ and heavy ions with up to 2 AGeV, opening up the possibility to investigate lepton and hadron physics in elementary and heavy ion collisions with HADES. Big emphasis lies on studying in-medium properties of mesons where the width and mass could be modified in nuclear environment at high densities ($\rho = (2-3) \cdot \rho_0$) and moderate temperatures ($T = 90\,\mathrm{MeV}$). Elementary processes, $p + p$, $\pi^- + p$ ($\rho = 0 \cdot \rho_0$), are investigated to serve as a reference for heavy ion collisions. Especially vector mesons are examined in normal nuclear matter ($\rho = \rho_0$) making use of light projectiles (p, π^-) on heavy ion targets, as well as in dense nuclear matter created by shooting relativistic heavy ions on heavy ion targets, since they act like a probe of the nuclear phase. Here in particular the rare decay channel of these light vector mesons into an e^+/e^- pairs is of great interest, because they are not influenced by the strong interaction.

HADES is composed several subsystems for particle identification, momentum and energy loss measurements. The schematic layout of all detector subsystems is shown in Fig. 2.2. The spectrometer consist of six identical sectors surrounding the beam axis with a large azimuthal acceptance of about 85% covering polar angles from $15° \leq \theta \leq 85°$.
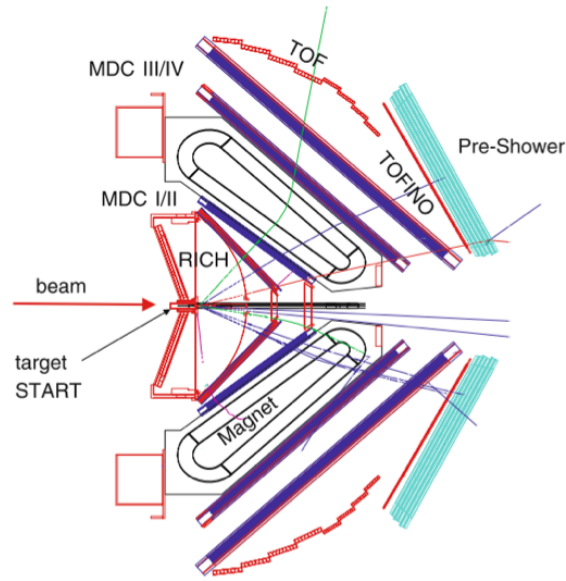
---

1   Schwerionen Synchrotron

Figure 2.2: Schematic of the HADES spectrometer with an angular coverage from $18° \leq \theta \leq 85°$ in forward direction. The beam is impinging on a Start detector, which is located in front of the target inside the beampipe surrounded by the Rich detector. The MDC are located before and after the superconducting magnet. Afterwards there are the Time-of-Flight detectors.

2.1 Start detector

The task of the Start detector is the definition of the T_0 for the Time-of-Flight measurement (time-resolution $< 50\,\mathrm{ps}$) as well as the identification of the beam properties and quality. During the secondary pion beam run the detector consisted out of an array of 9 diamond elements distributed on two Printed Circuit Boards (PCBs) (Fig. 2.3). Each diamond sensor has an active area of $4.6 \times 4.6\,\mathrm{cm}^2$ respectively $4.7 \times 4.7\,\mathrm{cm}^2$ and is divided into 4 segments. The thickness of $300\,\mathrm{\mu m}$ is a reasonable compromise between multiple scattering and signal-to-noise ratio. A diamond sensor stands out for high rate capability and radiation hardness, especially compared to silicon sensor, which suffer from radiation damage. It has moreover a fast signal collection time and low noise due to its rather large band gab energy of $5.5\,\mathrm{eV}$. [Fab13]
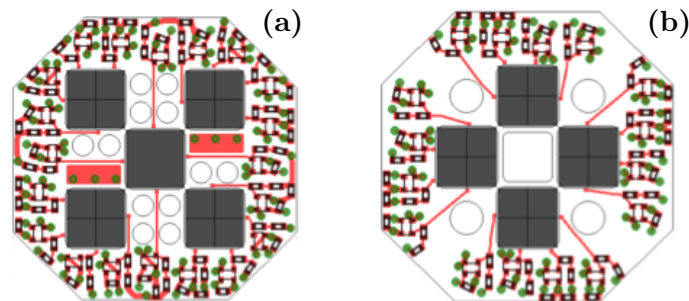
Figure 2.3: Top view of the diamond support PCBs (Printed Circuit Board) containing **(a)** five and **(b)** four diamond sensors, indicated in grey [Fab13].

2.2 Target

The fixed target is located inside the beamline in front of the Rich detector. Elementary reactions are investigated with a LH$_2$[1] target or like during the pion beam run with a polyethylene (H$_4$C$_2$) target. Whereas for $A + A$, $p + A$ or $\pi^- + A$ collisions segmented solid state targets were utilized. Drawings of all four targets that were employed during the whole pion beam campaign are depicted in Fig. 2.4, with the different features listed in Table 2.1.
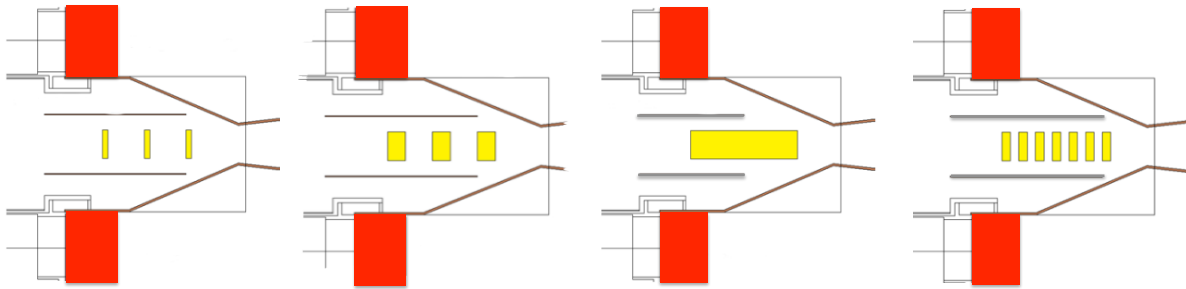

Figure 2.4: Drawing of the targets used during the pion-induced physics production run: **(a)** Tungsten, **(b)** Carbon, **(c)** Polyethylene, **(d)** Carbon.

Target	#Segments	#Diameter [mm]	Segment length[mm]
Tungsten (W)	3	12	2.4
Carbon (C)	3	12	7.2
Polyethylene (PE)	1	12	46
Carbon (C)	7	12	3.6

Table 2.1: Properties of all targets that were employed during both experimental campaign with the secondary pion beam.

2.3 Rich detector

The Rich[2] detector is used for the e^-/e^+ identification and based on the generation mechanism of Cherenkov light production. Charged particles traversing through the detector radiator gas, polarize the molecules that afterwards relax by emitting radiation. If the velocity of the particles is larger than the threshold velocity of the radiator (Eq. (2.1)), a coherent wave front builds up and Cherenkov light is created.

$$v = \beta \cdot c > \frac{c}{n} \equiv v_{thr} \qquad (2.1)$$

In the energy range of the SIS18 leptons travel with a velocity close to the speed-of-light ($\beta = v/c \sim 1$) were as hadrons are in the range of $\beta < 0.95$. By choosing a radiator with proper refractive index, the detector is hadron blind. The employed radiator gas of the Rich

---

1   liquid hydrogen
2   Ring Imaging Cherenkov

detector has a threshold of $\beta_{thr} < 0.997$, thus Cherenkov light is only created by electrons and positrons while passing the radiator gas. Then the light is reflected by a low mass carbon shell spherical mirror focussed to a ring, finally hitting the photosensitive CsI cathodes of the six Multi-Wire Proportional Chambers (MWPC). The ring information together with a reconstructed particle track is used to identify electrons and positrons. A schematic layout of the Rich detector is illustrated in Figure 2.5.
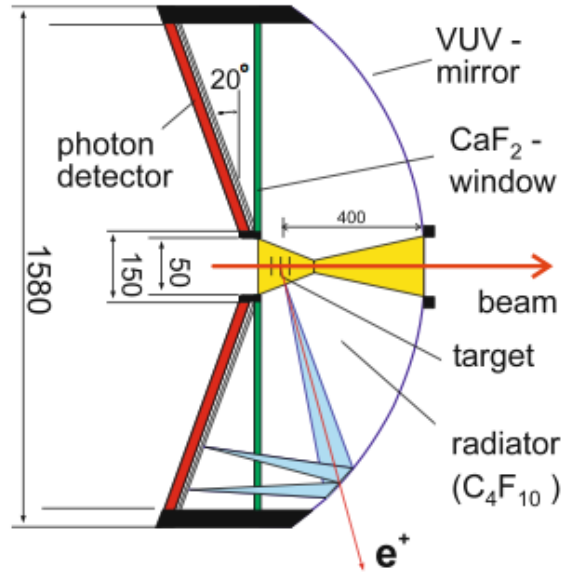

Figure 2.5: Drawing of the Rich detector. The Cherenkov light produced by the traversing positron is reflected on the mirror and focussed to a ring on the readout pads. [Aga09]

2.4 Multiwire Drift Chambers (MDCs)

The tracking of HADES is realized with four Multiwire Drift Chamber (MDCs) layers (I-IV) respectively two in front (I-II) of the toroidal magnetic field and two after (I-II). Each MDC layer is divided into six trapezoidal sector arranged symmetrically around the beam axis. All sectors have an azimuthal acceptance of 60° with sizes ranging from $88 \, \text{cm} \times 80 \, \text{cm}$ to $280 \, \text{cm} \times 230 \, \text{cm}$ of the most outer MDC layer. Each of the 24 MDC modules is composed of six drift cell layers with 27.000 cells in total such that the granularity is constant. Charged particles traversing the chambers ionize the gas molecules along their trajectory forming so called clusters. The thereby produced electrons are accelerated in the electric field generated between the cathode and anode wires, causing an electron cloud on the basis of the avalanche effect that finally introduce an electric signal, which is read out. In total four hit positions in the MDC layers are measured with the hit positions of the first two layers grouped together to an inner track segment and from the two others an outer one. With help of the Runge-Kutta method the equation of motion in the magnetic field region is solved in a recursive way using the hit position as initial condition.

2.5 Magnet

Charged particles traversing a magnetic field are deflected according to the Lorentz force, whereas the total momentum stays constant. The momentum of the particles can be obtained by measuring the deflection. The HADES spectrometer makes use of this principle by placing two layers MDC in front and after the magnet that measure the position of the passing particle. The magnets create a strong inhomogeneous toroidal magnetic field with field strengths from $0.9\,\mathrm{T} \leq B \leq 3.6\,\mathrm{T}$ at the sector edge. The magnet was build such that the target region as well as the active volume of the Rich detector is free of any magnetic field to not influence the particle reactions and identification of electrons and positrons.

Figure 2.6: Photograph of the superconducting toroidal magnet of HADES.

2.6 Time of Flight detectors

The main task of the Time-of-Flight detectors is to measure the hadron multiplicity, in order to trigger on the centrality of the collision. All three subsystems are part of the Multiplicity Electron Trigger Array system (META) and described in detail:

- **TOF**:
  The TOF wall consists of 6 sectors arranged in the same hexagonal geometry like the whole Hades setup. Each of these sectors is constituted of 8 modules containing 8 scintillator bars. A charged particle passing through the rod generates photon emission which is detected with PMTs[1] at both ends of the scintillator delivering the arrival time and pulse height. The time resolution is around $\sigma_{TOF} \sim 150\,\mathrm{ps}$ and the pulse height can be related to an energy loss, that can be used for particle identification.

- **TOFINO**:
  The TOFINO detector covers polar angles of $18° < \theta < 45°$. The system is divided in six sectors each constituted of four scintillator paddles of trapezoidal shape offering low granularity with an increased probability of double hits. The time resolution with $\sigma_{TOFINO} \sim 420\,\mathrm{ps}$ is worse than the resolution of the TOF detector.

---

1   Photo-Multiplier Tubes

- **Pre-Shower**:
  The Pre-Shower detector is located behind the TOFINO detector. Its is based on the electromagnetic shower creation of leptons and gammas traversing high Z materials and therefore used for the dilepton identification. Through the converter passing electrons/positrons generate Bremstrahlung which annihilates via pair production, a shower builds up. The detector consists of three wire chambers with two lead converters placed in between.

- **Resistive Plate Chamber (RPC)**:
  The RPC wall ESTRELA[1] replaced the TOFINO detector in an upgrade that started in 2009. It covers the low polar angle region $18° < \theta < 45°$ with full azimuthal coverage and a time resolution below $\sigma_{RPC} \sim 100\,\mathrm{ps}$ is achieved for a improved particle identification.

2.7 Forward Wall
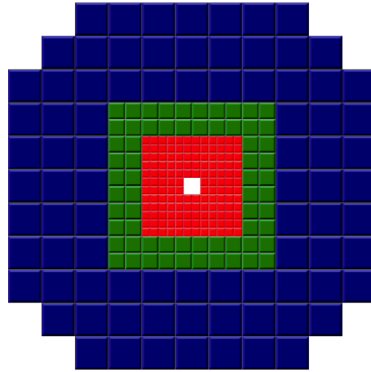
Figure 2.7: Schematic of the Forward Wall consisting out of 287 scintillator modules.

The Forward Wall was the first time installed in 2007 on the basis of the study of proton deuteron reactions. A feature of these reactions is the spectator nucleon moving in forward directions at small polar angles, which are not covered by the HADES detector systems ($15° \leq \theta \leq 85°$). The therefore build Forward Wall consists of 287 scintillator modules read out by PMTs and is located 7 m downstream the target with a polar acceptance of $0.33° < \theta < 7.17°$.

2.8 Hodoscope

The Hodoscope is located after the HADES detector system covering polar angles outside the acceptance of the spectrometer as well as of the Forward Wall. Therefore it is utilized as a beam monitor in order to control the y-position of the secondary pion beam. It is composed of 16 horizontally aligned plastic rods, that are read out on each side by a PMT (0.75 inch Hamamatsu R3478 PMT), leading to 32 readout channels in total.

---

1 Electrically Shielded Timing RPC Ensemble for Low Angles

2.9 Trigger decision

HADES is a triggered experimental setup, if the incoming beam particle interacts with the target nucleons in terms of scattering or creation of new particles, signals may be registered by the detector subsystems. These signals can be used as an input to the Central Trigger System (CTS) that transmits afterwards a trigger signal to all detectors. Since the HADES data acquisitions is based on a trigger-busy-release architecture, it is only possible to generate a new trigger signal after all subsystems are able to process the next event. In general the trigger decision is divided into two stages:

- **LV1 trigger**:
  The LV1 trigger condition requires at least one hit in the Start detector and two in the META system (TOF/RPC). This minimizes the contamination from random noise in the data. Only if the LV1 trigger condition is full-filled, the event is further processed by sending a trigger signal to all subsystems.

- **LV2 Trigger**:
  The LV2 trigger task is to enhance events containing e^+/e^- pairs. Therefore the online Imaging Units (IPUs) is searching for these pairs in the data words of the different subsystem, e.g the RICH detector. This trigger has not been employed in the experimental campaigns with pion beams.

If a positive trigger decision has been transmitted, all subsystems send there data to the Event-Builder (EB), which combines all the information from the detector systems to a common event structure and saves it on disk.

3 Principles of silicon sensors

3.1 Intrinsic silicon

Silicon, a semiconductor with a band gap energy of $E_g = 1.2\,\text{eV}$, has an indirect band gap leading to an energy of $3.6\,\text{eV}$ needed to create an electron-hole pair. Due to this rather low ionization energy these pairs can be already generated at room temperature. Besides that because of its intrinsic high density, a huge amount of charge carriers is produced by a traversing ionizing particle. Since these charge carriers can move nearly free inside the silicon material, the charge collection time is rather fast.

3.2 Extrinsic silicon

In intrinsic semiconductors electrons and holes are always generated pairwise. By doping, adding impurities inside the crystal lattice, such intrinsic properties can be changed. In general the doping is divided into to classifications: n- and p-type. N-type silicon is produced by inserting so called donors (e.g phosphorus) having an extra valence electron. This electron can be thermally released into the conduction band, leading to an increased amount of electrons in the conduction band compared to holes in the valence band and therefore they are called majority charge carriers. Apart from the case of p-type silicon, acceptors (e.g boron) with one valence electron less are added to the bulk material. Thus here the holes are the majority charge carriers.

3.3 p-n junction

By connecting two extrinsic semiconductors with opposite doping a p-n junction is generated, thanks to the recombination of electrons from the n-region and holes from the p-region in the transition area. The thereby left behind positively charged donor in the n-type material and negatively charged acceptor induce a potential difference, hence a space-charge region, called depletion zone. These charged acceptors as well as donors attract respectively the minority charge carriers leading to a drift current. Since the majority charge carriers diffuse in the opposite direction, in thermal equilibrium no net current is created. In addition such depletion zones can be also created at n^+-n and p^+-p transitions. By applying a negative potential at the p-layer the depletion zone is further increased, called reverse biased. Electron and holes generated in the depletion zone by traversing ionizing particles are attracted in opposite direction leading to a separation (Fig. 3.1). Therefore no recombination occurs, which is crucial for the operation of such sensors having the aim to collect the charges at the electrodes so that a signal is produced which can be readout.
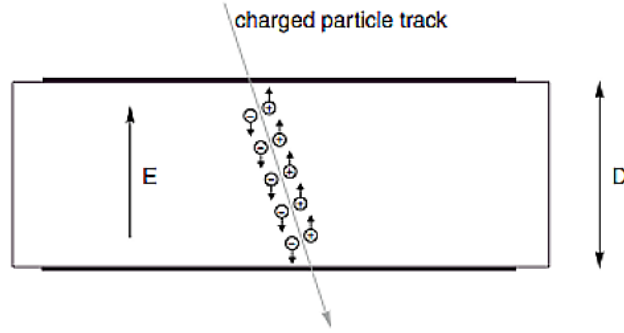
Figure 3.1: The free electron-hole pairs generated by a traversing ionizing particle along the track are attracted in opposite directions by the electric field [Fri01].

3.4 Energy loss of pions in silicon

Charged particles traversing through a medium transfer energy to the shell electrons of the atom. This transferred energy called energy loss is described by the Bethe-Bloch formula:

$$-\frac{1}{\rho}\frac{dE}{dx} = 4\pi N_A r_e^2 m_e c^2 z^2 \frac{Z}{A}\frac{1}{\beta^2}\left[\frac{1}{2}\ln\left(\frac{2m_e c^2 \beta^2 \gamma^2 T_{max}}{I^2}\right) - \beta^2 - \frac{\delta(\gamma)}{2} - \frac{C}{Z}\right],\qquad(3.1)$$

where ze is the charge of the traversing particle, N_A is the Avogardo's number , Z is the atomic number, A is the mass number, m_e is the mass as well as r_e is classical radius of the electron, T_{max} (Eq. (3.2)) is the maximum energy transfer in a single collision, I is the mean excitation energy of the material, $\beta = \frac{v}{c}, \gamma = (1-\beta^2)^{\frac{1}{2}}$, where c is the speed of light, $\delta(\gamma)$ is the correction for the shielding of the particle's electric field by the atomic electrons, referred to as density effect caused by the polarization of the atoms, C is the shell correction, because at low energies the basic assumption that the atomic electrons are static is not valid.

$$T_{max} = \frac{2m_e c^2 \beta^2 \gamma^2}{1 + 2\gamma m_e/M + (m_e/M)}\qquad(3.2)$$

In a thin detector layer the so-called restricted formula describes the corresponding energy deposition inside the detector, since $\delta-$electrons can be knocked-out from the active material leading to a smaller energy deposition than the mean energy loss (truncated Landau distribution):

$$-\frac{1}{\rho}\frac{dE}{dx} = 4\pi N_A r_e^2 m_e c^2 z^2 \frac{Z}{A}\frac{1}{\beta^2}\left[\frac{1}{2}\ln\left(\frac{2m_e c^2 \beta^2 \gamma^2 T_{max}}{I^2}\right) - \beta^2\left(1 + \frac{T_{upper}}{T_{max}}\right) - \frac{\delta(\gamma)}{2} - \frac{C}{Z}\right]\quad(3.3)$$

This results in a minimum energy deposition of $750\,\mathrm{GeV\,c^{-1}}$ in a $300\,\mu\mathrm{m}$ thick silicon layer instead of $450\,\mathrm{GeV\,c^{-1}}$, which is depicted in Fig. 6.22. Moreover the relativistic rise is deduced. Both effects have been confirmed by dedicated experiments at BNL by HEPHY and MIT (Fig. 3.3). [Fri01]
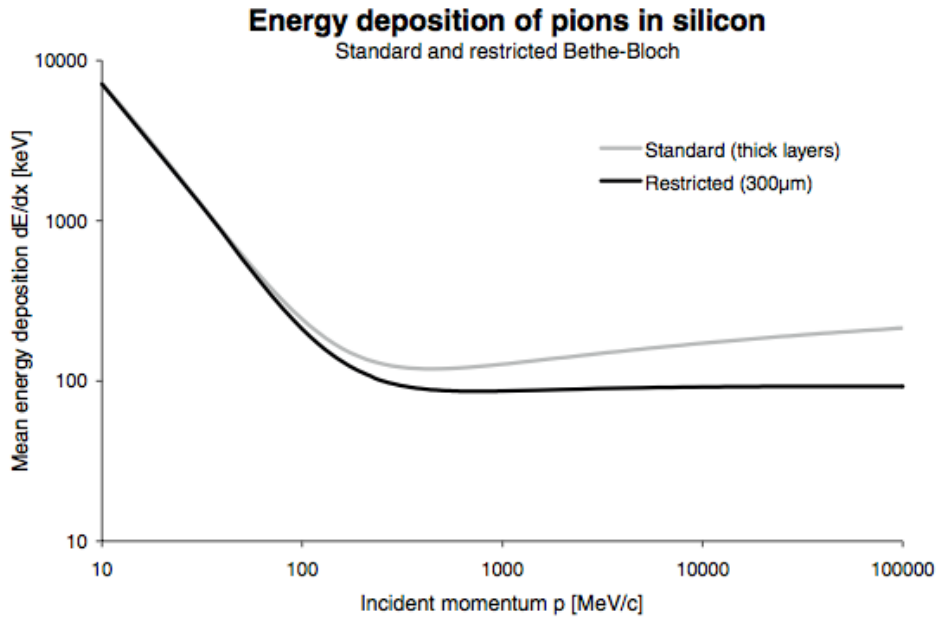
Figure 3.2: Energy deposition of pions traversing through silicon. A restriction of the standard Bethe-Bloch formula is applied for thin layers (300 µm) to account for energy carried away by energetic $\delta-$electrons [Fri01].
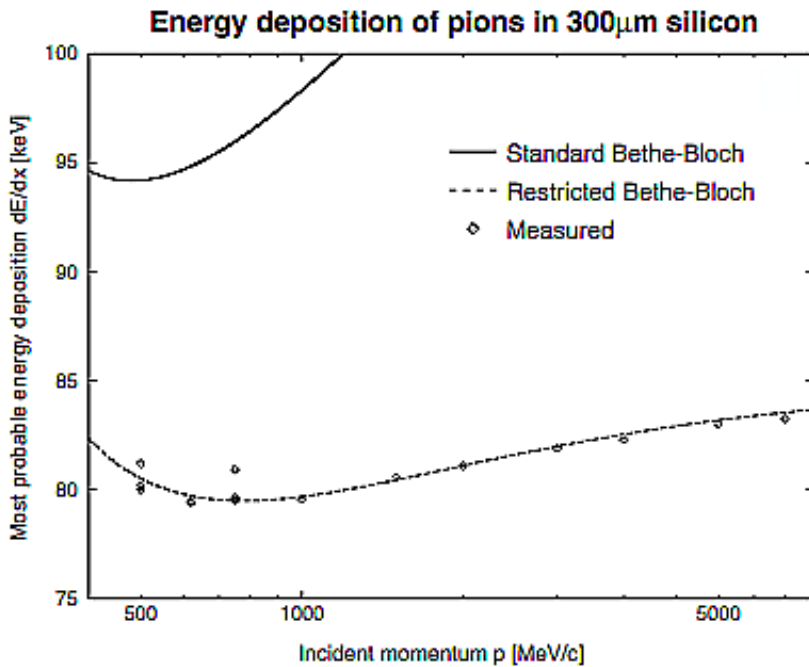
Figure 3.3: Calculated and measured most probable energy deposition of pions in 300 µm silicon sensor compared to the standard Bethe-Bloch theory [Fri01].

4 Concept of CERBEROS

In this chapter the basic concept according the mechanical layout, the employed detector as well as the acquisition electronics of CERBEROS (Central Beam Tracker for Pions) is discussed.

4.1 Basic Requirements

Secondary pion beams are produced by a high intensity Nitrogen beam (10^{11} part./s) impacting on a Beryllium target, leading a huge spread in both, momentum and angle, only limited by the intrinsic beamline acceptance of around $\Delta p/p \approx 8\%$. For an exclusive analysis it is mandatory to measure the momentum event by event with a resolution below 0.5 %. Therefore, CERBEROS, a secondary beam diagnostic system, was developed to allow for online beam monitoring as well as the momentum reconstruction of each individual pion at high beam rates (dN/dt $> 10^6$ part./s). CERBEROS consists of two tracking stations located at two different positions along the pion beam chicane (Fig. 1.8): the first one is located in the NE5 area and the second one in the HADES cave. Especially demanding is the employment of detectors with minimal multiple scattering and sufficient spatial resolution of every pion hit, since the momentum reconstruction is achieved on the basis of the four extracted hit positions and the beam optics transport calculations. Furthermore the detectors have to be operated under vacuum conditions (10^{-7} mbar).

4.2 Mechanical design of the vacuum chamber
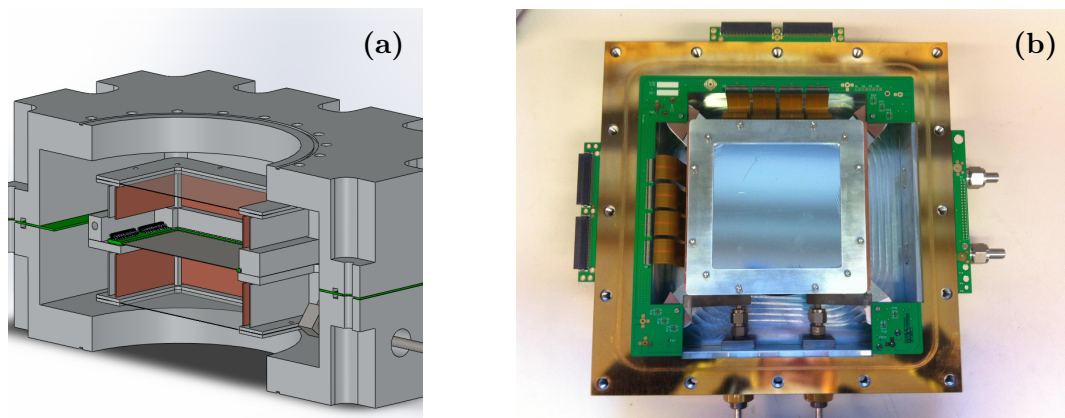
Figure 4.1: (a) Cross section of the vacuum chamber. It consists of two halves made of aluminium with a feed-through PCB sandwiched in between. The silicon sensor is located in the middle on a copper cooling body covered by Mylar foil. **(b)** Photograph of one half of the vacuum chamber with the silicon sensor covered by the Mylar window.

The tracking stations of CERBEROS are installed at two different locations along the pion beam chicane following the secondary pion beam from the pion production target to the HADES spectrometer (Fig. 1.8). Thus both silicon sensors must be placed in a vacuum (10^{-7} mbar) and light tight chamber integrated to the beam pipe mechanics. Both chambers are made of two identical aluminium blocks assembled face-to-face with a feed-through PCB placed in between for the signal routing to the FEBs (front-end electronics) (Fig. 4.1). The vacuum tightness between the blocks and the feed-through board is achieved by a o-ring positioned in a groove in each of the chamber halves. Two U-shaped frames can be attached to one of the halves, to mount the FEBs on them. Besides that, each chamber block has two additional vacuum-tight feed-through for the cooling fluid.

4.3 Silicon sensor

In Figure 4.2 (a) the employed radiation hard double sided silicon strip detector belonging to the TTT-3 series produced by MICRON SEMICONDUCTOR ltd is pictured. The sensor has a large active area of $10 \times 10\,\text{cm}^2$ covering most of the area inside the beamline. Having 128 strips on each side leads to a strip pitch of $760\,\mu\text{m}$. With a thickness of $300\,\mu\text{m}$ the multiple scattering is kept minimal. The radiation hardness is realized with a p-bulk (Fig. 4.2 (b)) and therefore no type-inversion is generated.
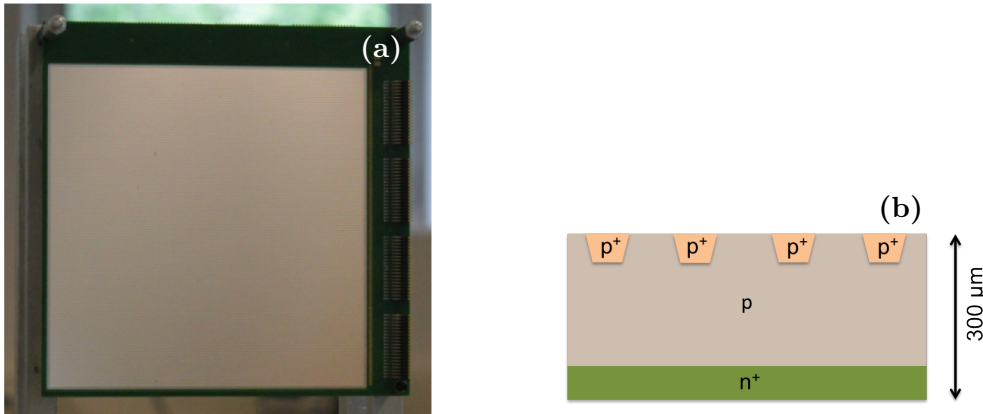
Figure 4.2: (a) Photograph of the radiation hard double sided silicon strip sensor. The $10\,\text{cm} \times 10\,\text{cm}$ sensor is glued to a PCB. Each of the 128 strips on each side is bonded to the corresponding pads on the PCB. The pads are routed to in total eight SAMTEC connectors with one row of four connectors on the right side of the PCB and the remaining four on the other PCB side on its top. **(b)** Illustration of a p-bulk type silicon sensor.

4.3.1 Detector cooling

The silicon sensor is operated at a temperature of about $-5\,°\text{C}$ realized with an indirect cooling via the PCB to which the silicon sensor is glued to. The main part of the cooling system consists of a copper cooling body (Fig. 4.3 (a)) on which the PCB is mounted. The cooling device is fluxed with a water-propylenglycole mixture (40:60) cooled down to $-20\,°\text{C}$ with a cooling bath thermostat MPC-K6s from Huber. To minimize the thermal losses of the whole system, the
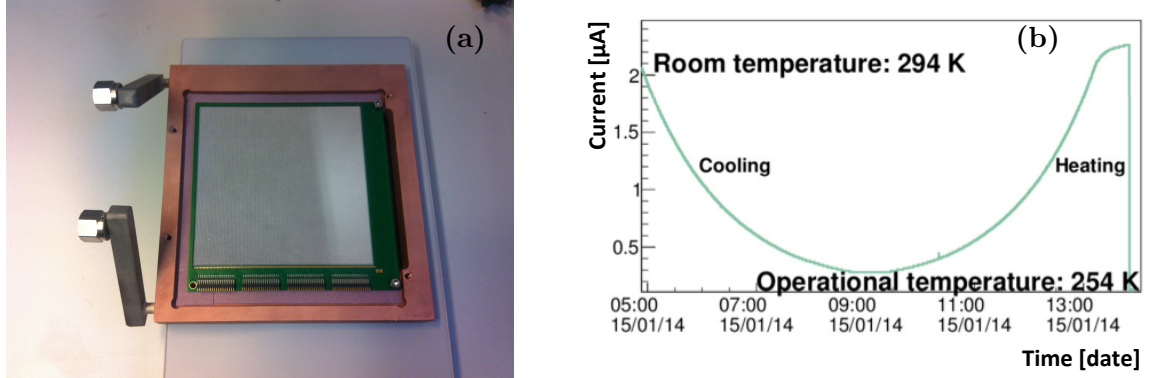
Figure 4.3: **(a)** Copper cooling body through which the cooling fluid is circulating, the PCB, on which the silicon sensor is mounted, is screwed to the copper. **(b)** Leakage current of the silicon sensor as a function of time during the cooling down and heating up process.

cooling tubes to the vacuum chamber are isolated. Besides that, a thermal heat conducting pad is placed between the PCB and copper block to guarantee a good heat transmission. Moreover, the heating up due to the incoming heat radiation from the surrounding vacuum chamber as well as from the beam pipes is reduced by copper plates, which are cooled down by the copper block, assembled vertically around the silicon sensor with two additional Mylar foils before and after (Fig. 4.1). The temperature of the silicon sensor was measured with a Pt100 sensor, which was slightly pressed on the surface of a mechanical sample.

One main aim of the cooling system was to decrease the leakage current and therefore the noise. According to theoretical predictions the leakage current has the following temperature dependent behaviour:

$$I(T) \sim T^2 \exp(-\frac{E_g}{2k_BT}), \tag{4.1}$$

where E_g is the band-gap energy (1.12 eV) [Bar93].

The actual temperature dependence of the leakage current of the silicon sensor mounted in the NE5 area can be seen in Fig. 4.3 (b). With a leakage current around 2 µA at room temperature an decrease to below 0.5 µA at the operation temperature of $-5\,°C$ (cooling fluid temperature: $-20\,°C$) is observed being bigger than the theoretical prediction ($\sim 0.21\,µA$).

4.4 Electronics and DAQ

This section includes the description of the readout system and the data acquisition (DAQ). The front-end part of the readout system is realized with the n-XYTER chip, which is read out by the TRB3 board integrating each tracking station in the HADES DAQ (Fig. 4.4). In HADES, all the detector systems (e.g. CERBERROS, Start) are controlled and monitored over one common network based on the TrbNet protocol by the central control system consisting of the CTS (Central Trigger System) and SCS (Slow Control System). The Slow Control System provides an interface for the operator to configure as well as monitor the detector. Whereas the CTS controls the trigger distribution and readout of the detector data. If a positive trigger decision has been
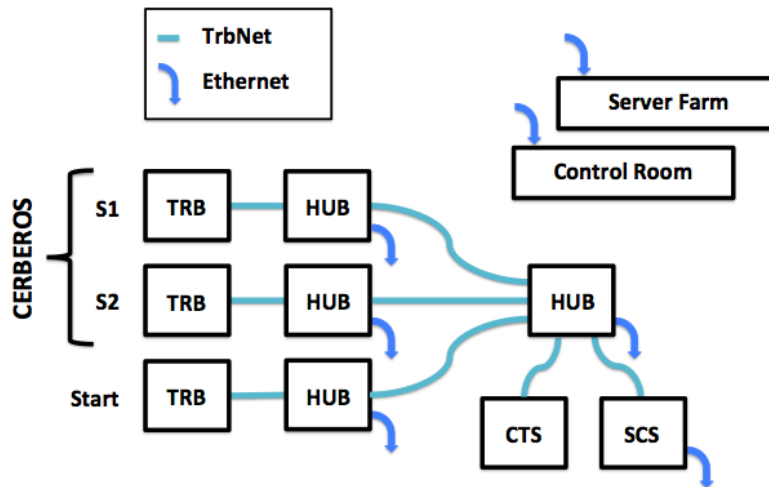
Figure 4.4: Simplified schematic of the HADES DAQ (data acquisition). The network has a tree-like structure based on the TrbNet protocol, connecting all detectors with the central control system (CTS and SCS). If a positive trigger decision has been transmitted, each sub-events recorded by the different detector systems is sent to the server farm (EventBuilder) over Gigabit Ethernet.

transmitted, each sub-event recorded by the different detectors is send to the EventBuilder (EB), which combines all the information to a common event structure and saves it on disk.

4.4.1 FEB: n-XYTER

Figure 4.5: The n-XYTER ASIC chip used as front-end electronics mounted on a aluminium cooling block.

The front-end board of the tracking system is realized with the n-XYTER ASIC[1] chip (Fig. 4.5), which was designed for experiments with neutrons by the DETINI collaboration. Its name stands for **N**eutron **X**, **Y**, **T**ime and **E**nergy **R**eadout. The chip works with positive as well as negative input charge polarities covering a dynamic input signal range of 6 MIPS each. Every chip offers 128 individual, self-triggered signal channels. The readout scheme of one single channel is depicted in Fig. 4.6, where the front-end part of the chip is realized for each channel individually. The signal generated by the particles passing the detector is first amplified in a charge-sensitive pre-amplifier. Further, the signal is split into two different signal processing circuits: the fast and slow chain.

---

1 Application-Specific Integrated Circuit

The fast chain is optimized for time measurements employing a fast shaper with a peaking time of 18.5 ns. Afterwards the signal reaches a comparator that is responsible for the self-triggering feature of this chip. If the signal amplitude is above the set threshold, it is tagged with a time stamp and buffered in the four level deep digital FIFO[1] together with the channel ID, overflow and pile-up bit. This time stamp gives the possibility to correlate front and back side of each silicon sensor as well as both tracking stations and has a resolution of about 1 ns governed by the resolution of the clock. Simultaneously, on the slow chain the signal passes the slow shaper dedicated for energy measurements with an ENC[2] of 12.7e/pF + 233e and a peaking time by the order of 100 ns. This shaper is followed up by a Peak Hold Detector detecting the signal's pulse height, which is then stored in a four level deep analogue FIFO. The back-end part is realized with a Token Ring Manager, that reads channel by channel checking the FIFO memory status and streams continuously the data out with a frequency of 32 MHz. The chip can cope with average hit rate per channel of 160 kHz with a dead time of 10 %. Since the energy information is encoded in the analogue pulse height, an external ADC[3] is needed. The control logic of the chip is realized via an I^{2}C[4] interface that controls various registers of the chip. There are 16 DAC[5] registers controlling the common biasing for different parameters of the pre-amplifier, shapers and peak-detectors for all channels. Another set of digital registers control the input polarity and readout modes. The chip can operate in four different modes as a combination of Test Pulse mode (analogue part) and Test Trigger mode (digital part) for the calibration and testing, while during the normal operation both are switched off. The general threshold setting for the comparator is common for all channels. Every channel can be masked for not delivering data to the back-end whereas the channel itself is working in its normal way. [Bro06]
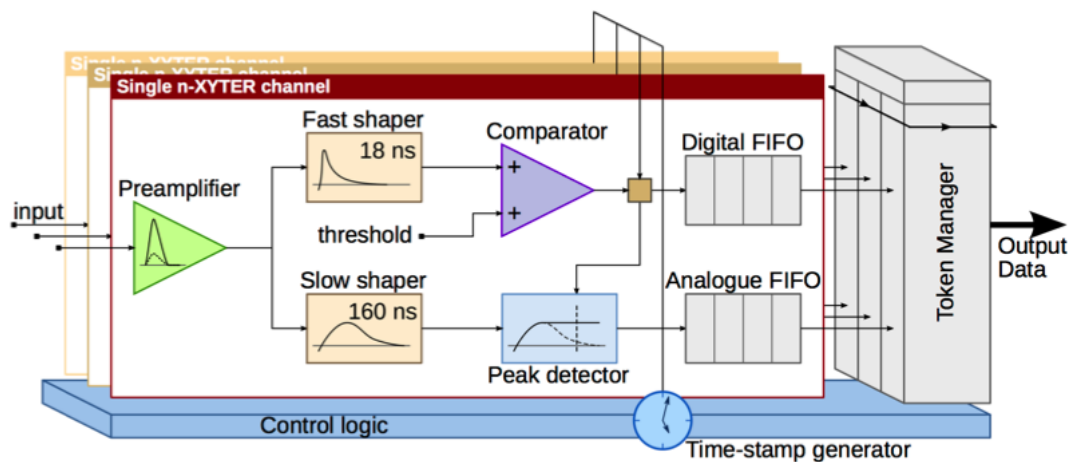
Figure 4.6: Schematic of the n-XYTER readout architecture. The front-end part is realized for each individual channel. The back-end part joins all channels (token ring architecture) and streams data to a single output bus. The DAC and time-stamp generator deliver common biasing and a time reference for all channels. [Lal15]

---

1   First In - First Out
2   Equivalent Noise Charge
3   Analogue-to-Digital Converter
4   Inter-Integrated Circuit
5   Digital-to-Analogue Converter

4.4.2 TRB3 board
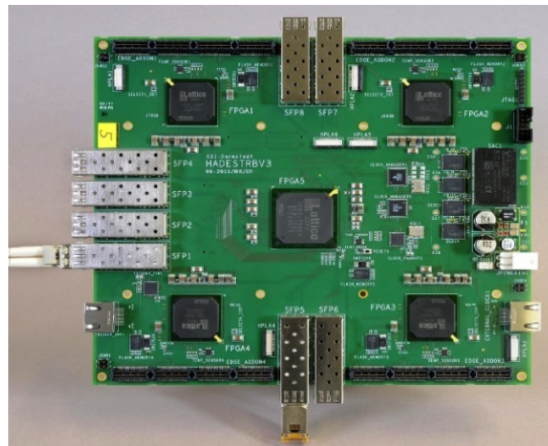
Figure 4.7: Photograph of the TRB3 board with its star like architecture of one central and four peripheral customizable FPGAs (Field Programmable Gate Arrays).

The readout chain is completed with the TRB3 board (Fig. 4.7). The TRB3 board with its star like architecture of one central and four peripheral user programmable FPGAs allows for the integration of the tracking system to complex detector systems like the HADES spectrometer as well as for a standalone system with the trigger decision unit running on the central FPGA. The slow control and data transfer is running over a GbE[1] connection which guarantees for data transfers up to 50 MBytes/s. A maximal trigger rate of up to 700 kHz is achieved by the low latency of the trigger processing leading to a low dead time. Each of the peripheral FPGAs offer 208 I/O pins. [Tra11]

All the data stored in the FIFO of the n-XYTER are read out by the TRB3 and stored in a register waiting for the request of the CTS[2] of the HADES DAQ. Only events within the time window (400 ns) of studied physical events in the HADES spectrometer are selected by the trigger logic on the board and send to the Event Builder (Fig. 4.8).
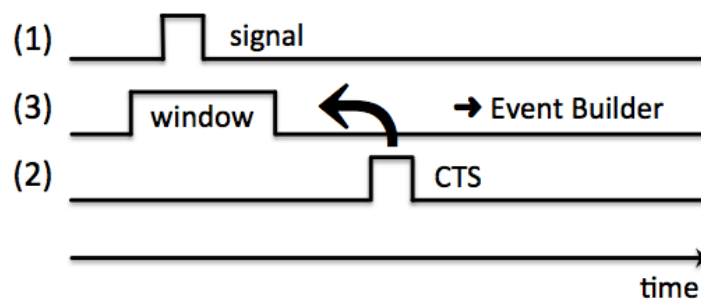
Figure 4.8: Schematic of the time window selection implemented on the TRB3 board. (1) The signal stored in the n-XYTER FIFO is read out and buffered in a register on the TRB3. (2) After a positive trigger decision distributed by the CTS the signal is further processed. (3) If the signal is within the time window, it is selected by the trigger logic and send to the Event Builder.

---

1   Gigabit Ethernet
2   Central Trigger System

5 Data analysis

The analysis framework of HADES, HYDRA2, adapted from ROOT is written in C++. It is an event based environment containing the original data, raw data, recorded by the detector subsystem as well as more elaborated data, resulting from several reconstruction processes. In Figure 5.1 the data analysis structure of CERBEROS is illustrated. As usual the first data set contains the raw data, which is then calibrated in terms of time and ADC value. The thereby obtained calibrated data is filtered by the hit-finder, that merges the front and back side of each sensor as well as reduces the background originating from events where the pions are not transmitted until the HADES target, and detector noise. Afterwards the track-finder is applied. This combines hits in the first and second tracking station to evaluate the momentum of the secondary pions on the basis of the beam optics transport code.
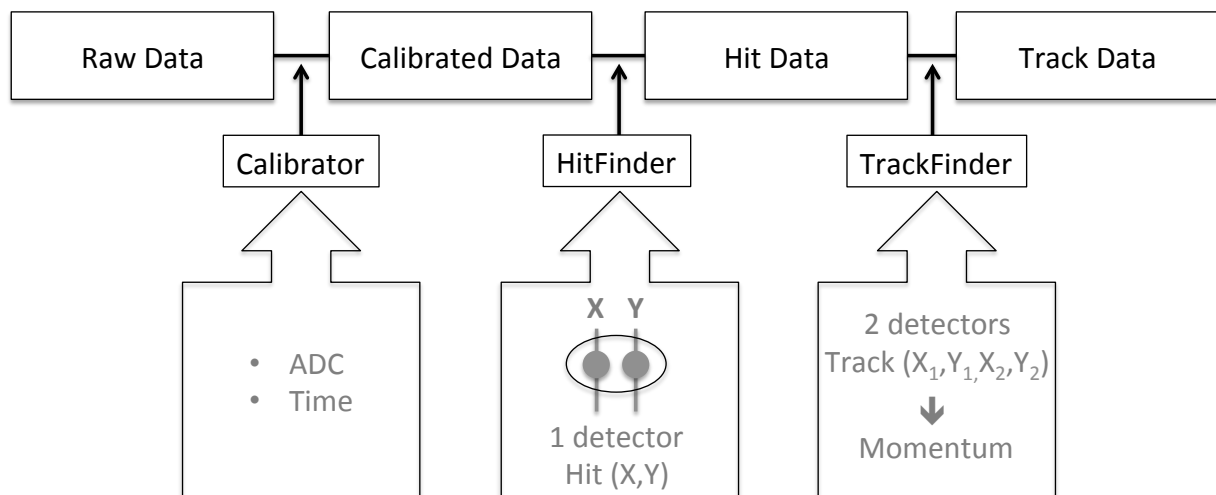
Figure 5.1: Scheme of the data analysis stages of CERBEROS implemented in the HYDRA2 framework of HADES.

5.1 Collected data

The total statistics collected during the first pion beam campaign is listed in Table 5.1, whereas the obtained data at a central beam momentum of $1.7\,\mathrm{GeV/c}$ is discussed in this work especially regarding the reconstructed hits of the front and back layer of each sensor as well as the reconstructed momentum. Both targets, Tungsten and Carbon, are treated simultaneously.
Concerning the second physics production run with the secondary pion beam (Table 5.2), the main focus is on the data obtained at a central beam momentum of $0.690\,\mathrm{GeV/c}$ with the employed polyethylene target (H_4C_2). Here the hit and momentum reconstruction are investigated. Whereas

the reconstructed momentum is analysed further in terms of the elastic scattering events. Nevertheless the other central beam momenta (0.656 GeV/c, 0.748 GeV/c, 0.800 GeV/c) are discussed as well.

Due to not stable beam conditions at the beginning of both pion beam experimental campaigns, these files are excluded from this analysis.

Target	RefMom [GeV/c]	Sum Events	Sum Runs
Tungsten (W)	1.700	128.5M	95
Carbon (C)	1.700	102.6M	76
Carbon (C)	0.700	5.1M	5
Polyethylene (PE)	0.700	93.2M	112

Table 5.1: Collected statistics for the first pion beam run.

Target	RefMom [GeV/c]	Sum Events	Sum Runs
Polyethylene (PE)	0.690	774.7M	2700
Polyethylene (PE)	0.748	76.5M	269
Polyethylene (PE)	0.656	42.4M	167
Polyethylene (PE)	0.800	52.4M	188
Carbon (C)	0.612	47.8M	179
Carbon (C)	0.690	60.7M	217
		55.0M	212
Carbon (C)	0.800	41.2M	146
Carbon (C)	0.748	42.2M	151
Carbon (C)	0.656	41.9M	521

Table 5.2: Collected statistics for the second pion beam campaign.

5.2 Pion beam rates

In Figure 5.2 the hit rate [Hz] as a function of time [s] on the x- and y-side of the first sensor (y-side: blue line, x-side: red line) and second sensor (y-side: green line, x-side: orange line) is shown at a central beam momentum of 1.7 GeV/c. The first tracking station had to cope with hit rates up to 7 MHz. Whereas the second one had to cope with lower hit rates up to 800 kHz, due to transmission losses of the pions along the pion beam chicane (Fig. 6.2 (a)).

During the second experimental campaign (0.690 GeV/c) even higher hit rates were reached on all four layers of the two tracking stations (Fig. 5.3). The first sensor had to cope with a maximal hit rate of up to 12 MHz and the second one up to 2 MHz.

However, throughout both experimental campaigns the hit rates were fluctuating, because of difficulties with the beam extraction of the SIS18 as well as due to too high radiation levels in the experimental hall.

01:29:21
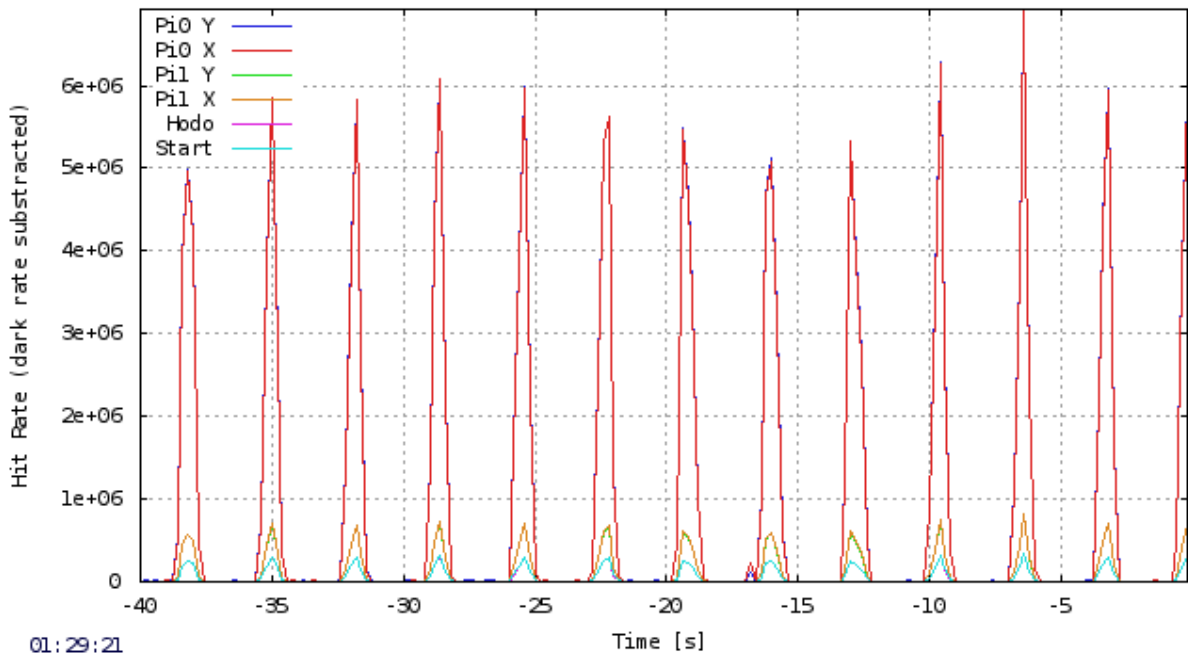
Figure 5.2: Hit rate [Hz] (dark rate subtracted) as a function of time [s] of the four pion tracker layer (P0 Y, P0 X, P1 Y, P1 X), Start detector and Hodoscope at a central beam momentum of 1.7 GeV/c [Mic15].

06:36:11
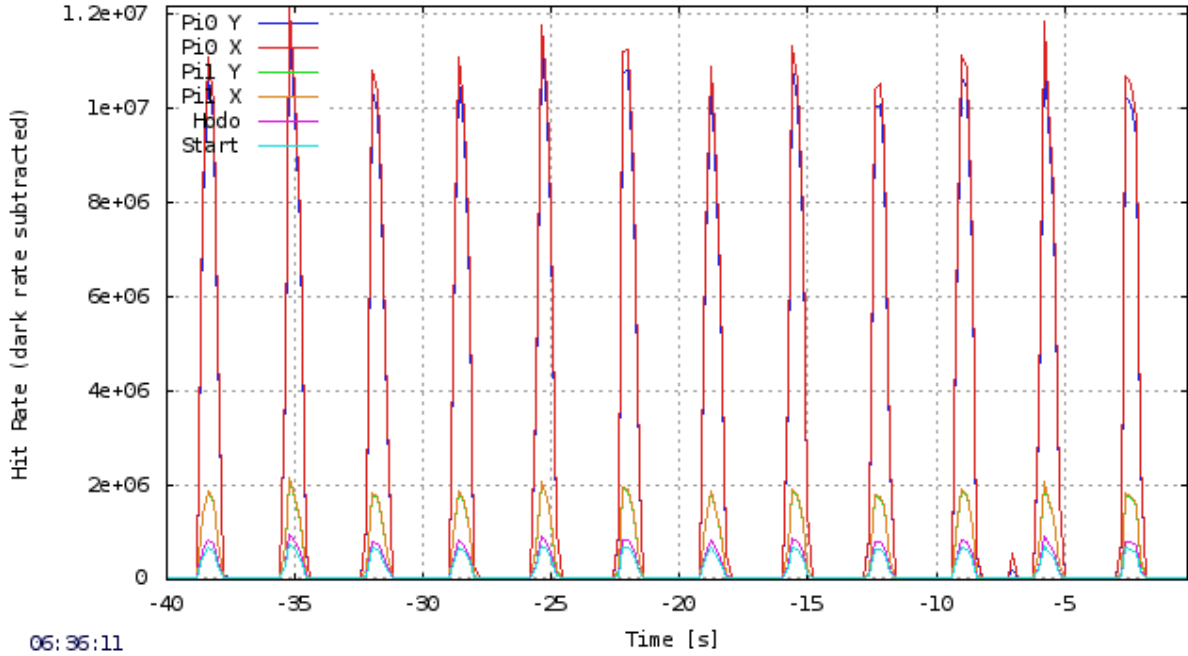
Figure 5.3: Hit rate [Hz] (dark rate subtracted) as a function of time [s] of the four pion tracker layer (P0 Y, P0 X, P1 Y, P1 X), Start detector and Hodoscope at a central beam momentum of 0.690 GeV/c [Mic15].

5.3 Raw Data

In Figure 5.4 the beam profiles on the first and second tracking station at a central beam momentum of $1.7\,\mathrm{GeV/c}$ are shown as a function of the strip number. On the first one a quite broad distribution in the x-direction with the beam maximum nicely centred in the middle can be seen, whereas in the y-direction a smaller region is covered. Contrary, the beam is spread nearly all over the whole sensor located in the HADES cave. By comparing the beam profiles to the one obtained at a central beam momentum of $0.690\,\mathrm{GeV/c}$ (Fig. 5.5), a shift of the beam maximum to lower strip numbers in the x-direction is observed on the detector mounted in the NE5 area. In contrast, the beam profiles on the second one (HADES cave) differ only slightly. During both experimental campaigns two strips on the y-side of the second sensor were broken, which is visible as horizontal lines in the plots.
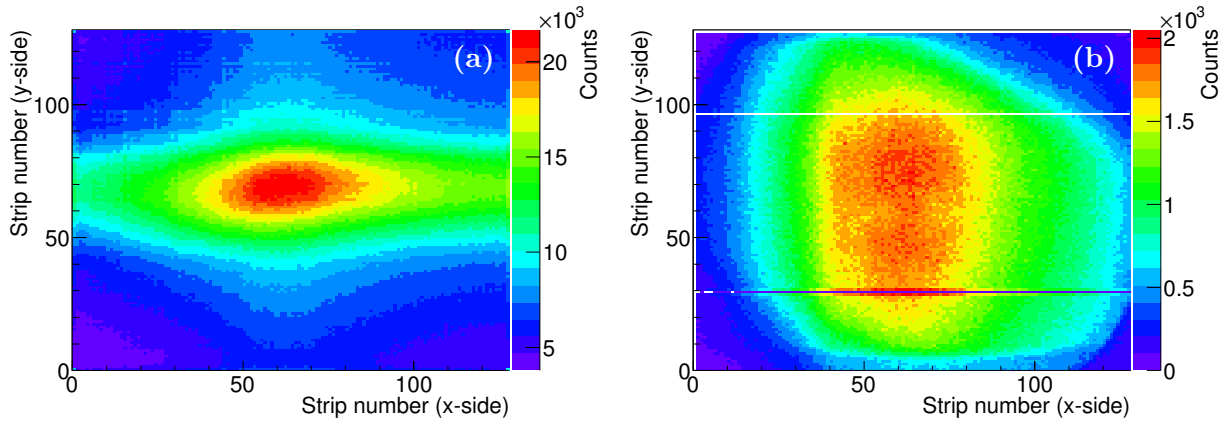
Figure 5.4: Beam profile on the two detector stations at a central beam momentum of $1.7\,\mathrm{GeV/c}$ **(a)** in the NE5 area with a broad distribution in the x-coordinate with the beam maximum nicely centered and **(b)** in the HADES cave, the beam is illuminating the sensor almost homogeneously.
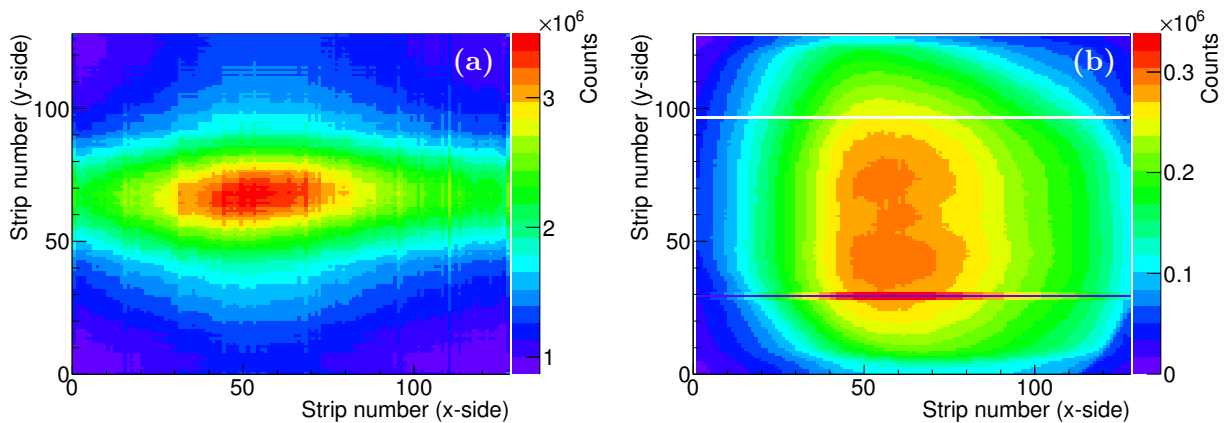
Figure 5.5: Beam profile on the two detector stations at an central beam momentum of $0.690\,\mathrm{GeV/c}$ **(a)** in the NE5 area and **(b)** in the HADES cave . The distribution on the first sensor there is broad in the x-coordinate with the beam maximum shifted to lower strip numbers. The distribution on the second one is rather homogeneous.

Besides the position information, the system delivers also a time stamp with respect to the CTS. Only events within a 400 ns time window with respect to the reference time delivered by the CTS have been selected. The distribution of the time stamp [ns] is depicted in Fig. 5.6 (a) (1.7 GeV/c) being clearly correlated with the CTS with a mean value of 180 ns and a resolution (σ) of around 9 ns. Besides the possibility to select only pion interacting with the target material, the time information offers the possibility to correlate front and back layer of each sensor (Fig. 5.6 (b)). The time correlation is more clear for the data collected with a central beam momentum of 0.690 GeV/c (Fig. 5.7 (b)), since for this setting the correlation line is more pronounced due to the contribution of pions that are not transported along the whole pion beam chicane. Moreover, the data taken during the second pion beam run was more affected by uncorrelated noise corresponding to the horizontal line and vertical line visible in Fig. 5.7 (b) in the range of the correlation peak (Fig. 5.7 (a)).
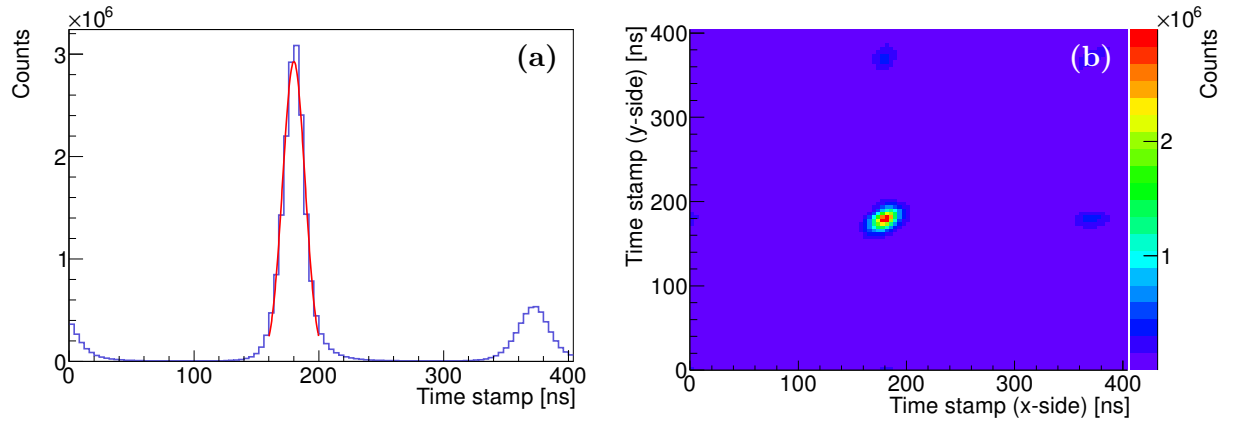
Figure 5.6: Timestamp in ns at a central beam momentum of 1.7 GeV/c with a time window of 400 ns: **(a)** time-correlation-peak with the CTS on the x-side of the first detector and **(b)** time correlation between front- and back-side of the first detector, where the timestamp of the x-side of the detector is plotted on the x-axis.
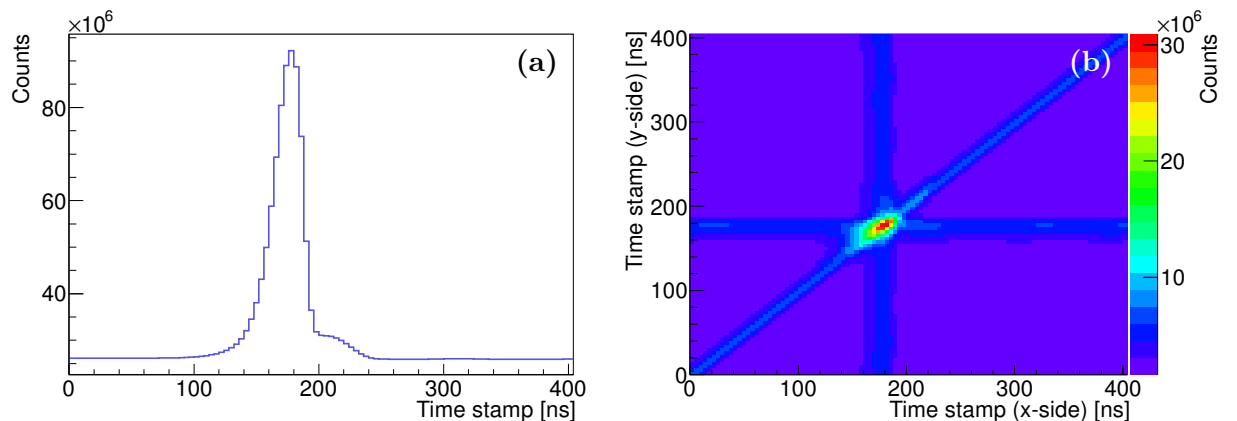
Figure 5.7: Timestamp in ns at an central beam momentum of 0.690 GeV/c with a time window of 400 ns **(a)** Time-correlation-peak with the CTS on the x-side of the first detector and **(b)** Time correlation between front- and back-side of the first detector, where the timestamp of the x-side of the detector is plotted on the x-axis.

The raw hit multiplicity distributions deliver a first impression on the upper limit of the relative efficiency achieved with all four pion tracker layers, since due to the LV1 trigger the data is only recorded, if there was at least one hit in the Start detector and two in the META system (TOF/PPC) as well. By looking at the raw hit multiplicity of the x-side of the first detector (Fig. 5.8 (a) at 1.7 GeV/c), one observes only a small amount of events with no registered hit. Therefore, the upper limit is 98.6 %. At a central beam momentum of 0.690 GeV/c the upper limit of 99.6 % is even bigger (Fig. 5.9 (b)) due to a larger contamination of background coming from uncorrelated noise. This is especially visible by comparing the multiplicity correlations, Fig. 5.8 (b) (1.7 GeV/c) and Fig. 5.9 (b) (0.690 GeV/c) of front and back layer (NE5 detector).
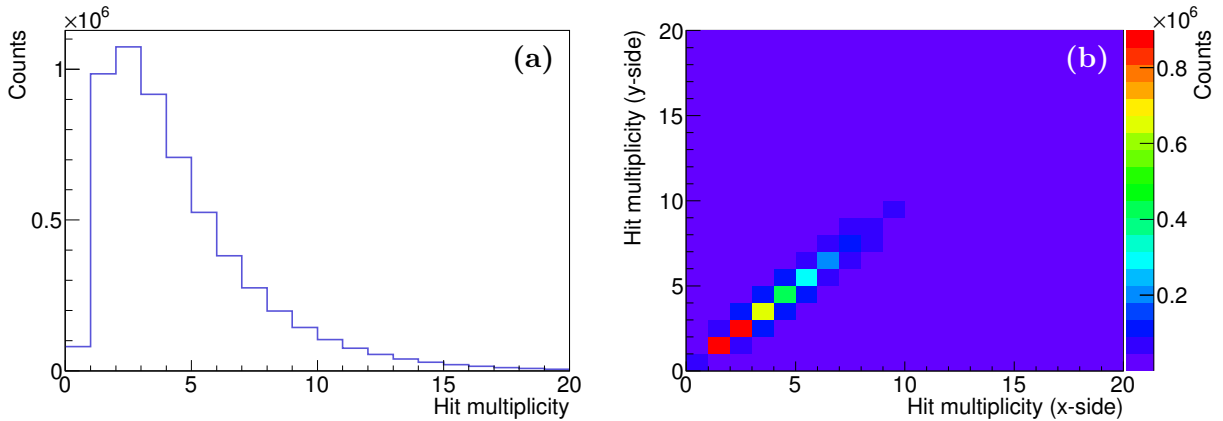
Figure 5.8: Raw hit multiplicity at a central beam momentum of 1.7 GeV/c within the 400 ns time window **(a)** on the x-side of the first detector and **(b)** showing the hit multiplicity correlation between front- and back-side of the first detector, where the hit multiplicity of the x-side of the detector is plotted on the x-axis.
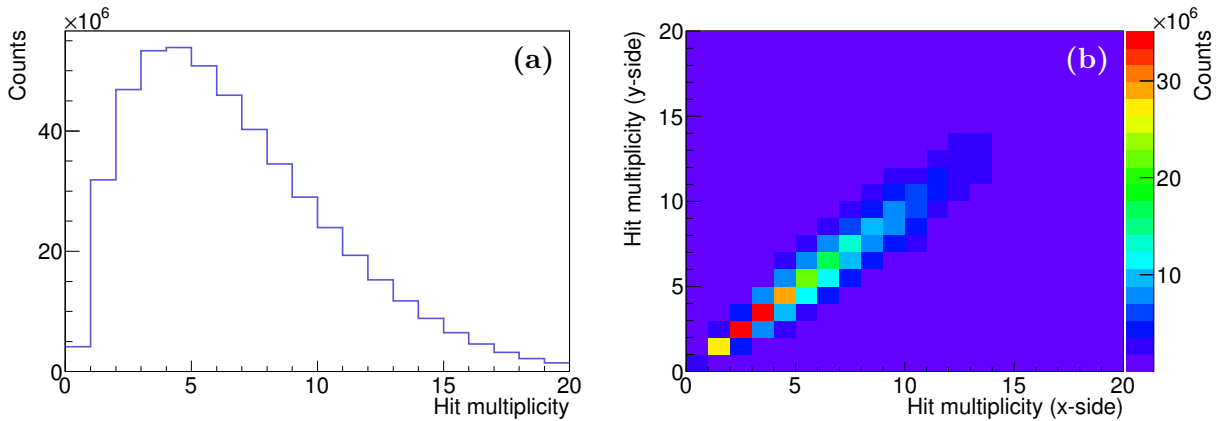
Figure 5.9: Raw hit multiplicity at a central beam momentum of 0.690 GeV/c within the 400 ns time window **(a)** on the x-side of the first detector and **(b)** the hit multiplicity correlation between front- and back-side of the first detector, where the hit multiplicity of the x-side of the detector is plotted on the x-axis.

5.4 Calibrated Data: calibration procedure

5.4.1 Time calibration

Figure 5.7 (a) shows time distribution of the raw data at the central beam momentum of 0.690 GeV/c. The results by a Gaussian Fit gives a mean value centered around 175 ns. During the calibration procedure the mean value of this distribution is extracted and afterwards shifted to zero to account for an arbitrary offset introduced by a change of cabling of the Start detector after the target exchange. The obtained calibrated time distribution is depicted in Fig. 5.10.
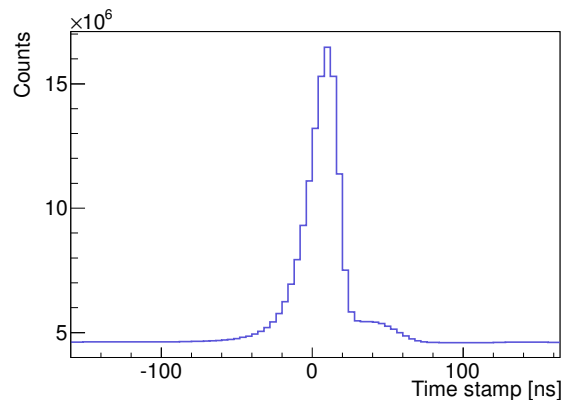
Figure 5.10: Calibrated time distribution of the x-side of the first tracking station at the central beam momentum of 0.690 GeV/c, centred around zero.

5.4.2 ADC calibration: baseline correction

In Figure 5.11 (a) the ADC values are plotted as a function of strip number for the raw data. Typical for the internal structure of the n-XYTER is the inverted ADC distribution as well as the curved shape originating from the varying baseline of each channel. Hence, a correction of the baseline with help of pedestal files taken in the Test Trigger mode with no threshold set at the discriminator has to be applied. Here the mean of the ADC distribution of the pedestal file is extracted and shifted to zero. Afterwards, the MPV[1] of the distribution is moved according to the shift of the pedestal and inverted. Since the pedestal file was recorded at the beginning of the beamtime, a correction of the temperature drift has to be included as well. Thus a data file close in time and temperature to the pedestal is taken as a reference. A common offset for all channels due to temperature changes is extracted based upon the difference of the MPV in the reference file to the MPV of all others. This procedure is performed for each n-XYTER individually. The corrected ADC values in terms of baseline and temperature drift as a function of strip difference are depicted in Fig. 5.11 (b).

Figure 5.12 shows the energy spectrum recorded during the whole experimental campaign at a central beam momentum of 1.7 GeV/c for all channels. As expected a Landau distribution is observed, since the measured energy loss is lower compared to the mean energy loss, which is due to δ-electrons leaving the active volume and not fully contributing to the energy loss (Section 3.4).

---

1 Most Probable Value

As a result of the internally set threshold of the n-XYTER no noise peak is visible, thus the MIP signal is nicely separated.
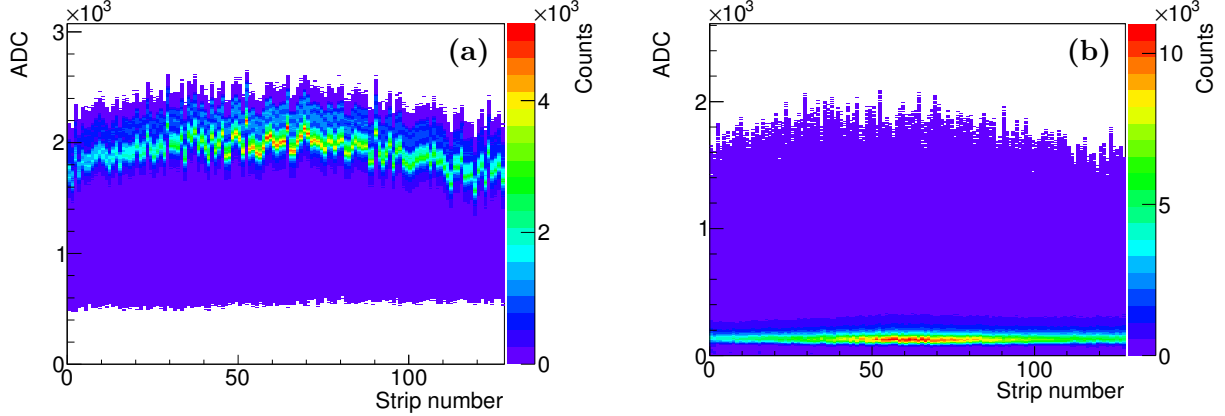
Figure 5.11: Obtained ADC value at a central beam momentum of $1.7\,\mathrm{GeV/c}$ **(a)** before and **(b)** after the calibration procedure as a function of strip number for the x-side of the first tracking station.
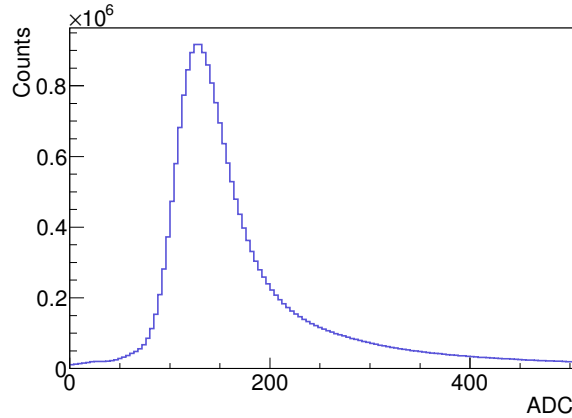
Figure 5.12: The calibrated ADC value at a central beam momentum of $1.7\,\mathrm{GeV/c}$ as a projection of all strips of the first x-position layer.

5.5 Hit Data: correlation method

The hit-finder associates the x- and y-positions of each double sided silicon sensor and the procedure is divided into two stages. The first one makes use of the time and strip number information only, whereas in the second stage the ADC information, if available, is included as well.

During the whole first pion beam run the ADC information is available for both tracking stations. Contrary, in the second one the ADC synchronisation between the n-XYTER and the TRB3 board of the detector mounted in the NE5 area was not functional anymore. Hence, the ADC values are only accessible for the HADES cave station. Thus, the first step of the hit-finder is demonstrated on the basis of data collected at a central beam momentum of $0.690\,\mathrm{GeV/c}$ and the second step by means of data at $1.7\,\mathrm{GeV/c}$.

Besides, on the hit-finder stage the position is converted from strip number into cm using:

$$position \; [\mathrm{cm}] = (position \; [\mathrm{stripnumber}] - 63.5 \; [\mathrm{stripnumber}]) \cdot \frac{0.076 \, \mathrm{cm}}{\mathrm{stripnumber}}, \tag{5.1}$$

where 0.076 cm represents the strip pitch of the silicon sensor.

5.5.1 Correlation 1: time and position information
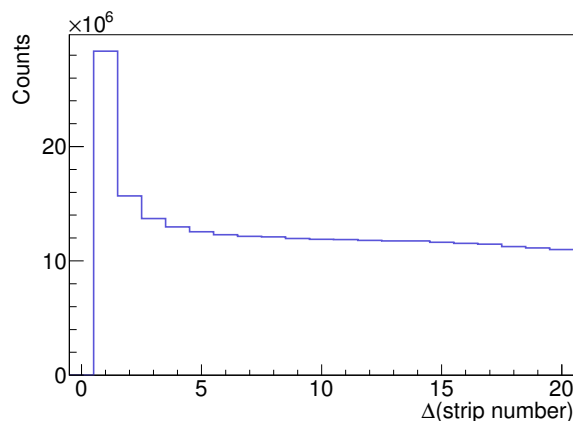
Figure 5.13: Distribution of the strip number difference between front and back side in the same event of the first detector. Both at a central beam momentum of 0.690 GeV/c.

Only events correlated with the CTS of the HADES detector system, thus events of studied physical reactions, are of interest. Since the time window of accepted events with 400 ns is quite broad as can be seen in Fig. 5.10, a cut around the correlation peak ranging from $-40 \, \mathrm{ns} \leq t \leq 20 \, \mathrm{ns}$ (1.7 GeV/c: $-30 \, \mathrm{ns} \leq t \leq 30 \, \mathrm{ns}$) is applied. Nevertheless this leaves still some noise contribution in the sample. If two or three nearby strips are in one event (Fig. 5.13 (b)), they are merged together and treated as one hit. A cut on the time difference between the front and back layer from $-30 \, \mathrm{ns} < \varDelta t < 30 \, \mathrm{ns}$ cleans the data further. This can be seen by comparing Fig. 5.14 (a) ($\sigma = 8.0 \, \mathrm{ns}$), where only events with just one hit in all four layers are plotted, with Fig. 5.14(b) ($\sigma = 13.2 \, \mathrm{ns}$), where all events are displayed with an already applied cut on the correlation peak. Since the time resolution of the whole readout chain is not sufficient to unambiguously correlate hits belonging together, all possible combinations (Fig. 5.15) have to be taken into account. This results in multiple hit candidates (Fig. 5.16). This way fake hits might be build by either combining real hits that do not belong together in events with multiple hits on each side or combining noise hits with real ones. In total a relative hit efficiency of 86.5 % for the detector located in the NE5 area and of 90.2 % for the one in the HADES cave is achieved. This difference is due to the larger noise rate of the NE5 station that leads to a larger busy time for the system and hence to a loss of events. Both efficiencies result then into an overall track efficiency of 78.4 % for both tracking stations (Fig. 5.17) with pion rates up to 12 MHz on the first sensor and up to 2 MHz on the second one.
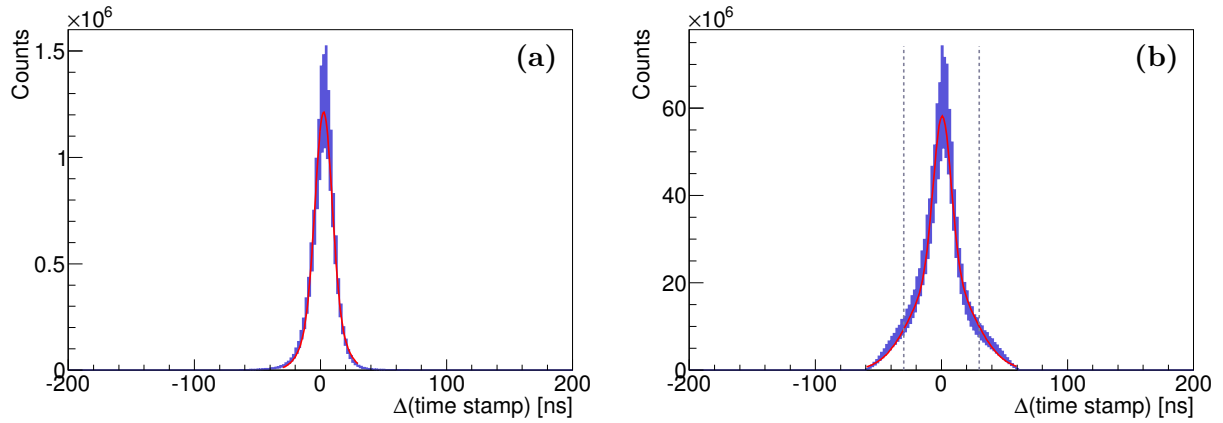
Figure 5.14: Time difference of front and back side for **(a)** events with only one hit in all four layers **(b)** for all hit multiplicities with a cut on the time correlation ($-40\,\mathrm{ns} \le t \le 20\,\mathrm{ns}$). Both at a central beam momentum of $0.690\,\mathrm{GeV/c}$.
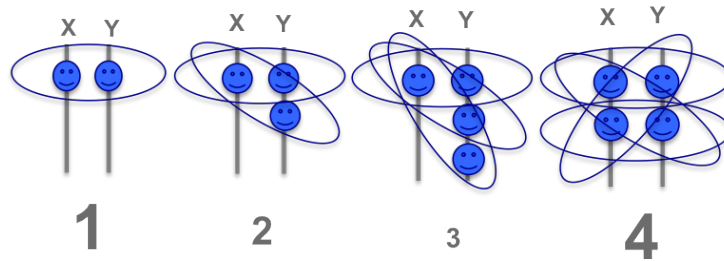
Figure 5.15: Schematic of possible combinations of the x- and y-positions of one sensor for real and noise hits.
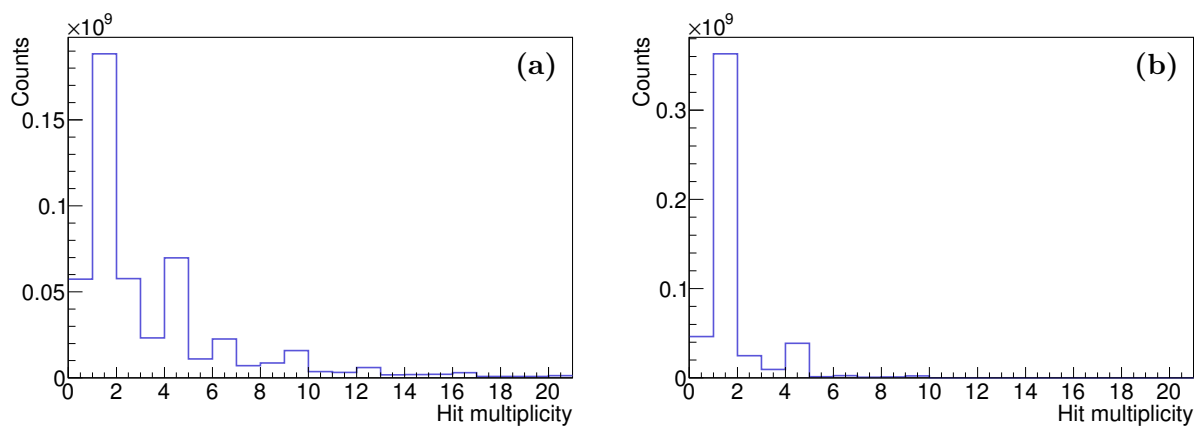
Figure 5.16: Hit multiplicity at the central beam momentum of $0.690\,\mathrm{GeV/c}$ with the correlation of front and back layer only based on the time and position information **(a)** for the first (NE5) and **(b)** for the second (HADES cave) tracking station.
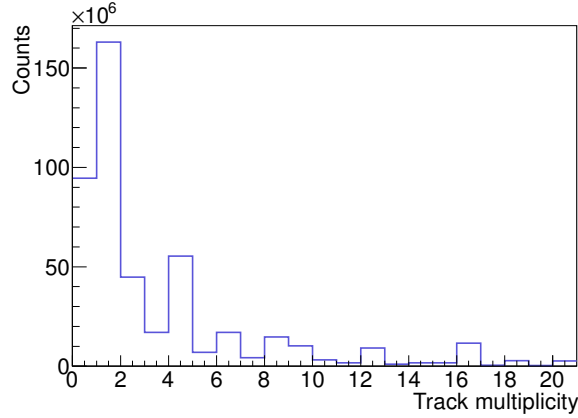
Figure 5.17: Track multiplicity at a central beam momentum of $0.690\,\mathrm{GeV/c}$ with the correlation of front and back plane of each sensor based only on the time and position information.

5.5.2 Correlation 2: time and ADC information

Since the electrons and holes are generated always pairwise by the traversing pions through the silicon sensor, the ADC information helps to further correlate both detector sides. In Figure 5.18 the difference in ADC channels of front and back side for the selected sample, where only events with just one hit in all four layers were chosen, is shown. By applying a cut on this difference ranging from $-43.98 < \Delta ADC < 29.02$, the data sample is cleaned up additionally. The final merging of the x- and y-positions is based on both, time and ADC information. Iteratively, front and back layer combinations with the smallest time and ADC difference ($r = \sqrt{\Delta t^2 + \Delta ADC^2} \rightarrow min$) are selected simultaneously. In Figure 5.19 (a) and (b) the obtained hit multiplicities are depicted with a relative hit efficiency of 92.5 % in the first station with hit rates up to $7\,\mathrm{MHz}$ and of 93.2 % in the second one with hit rates up to $800\,\mathrm{kHz}$ leading to a track efficiency of 87.0 %.
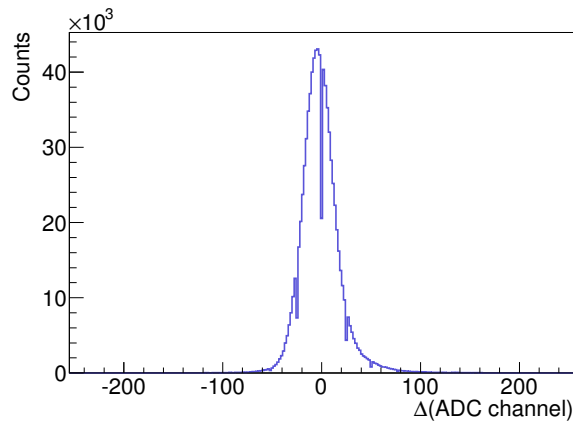
Figure 5.18: Difference in ADC value of front and back side of the first tracking station for a central beam momentum of $1.7\,\mathrm{GeV/c}$.
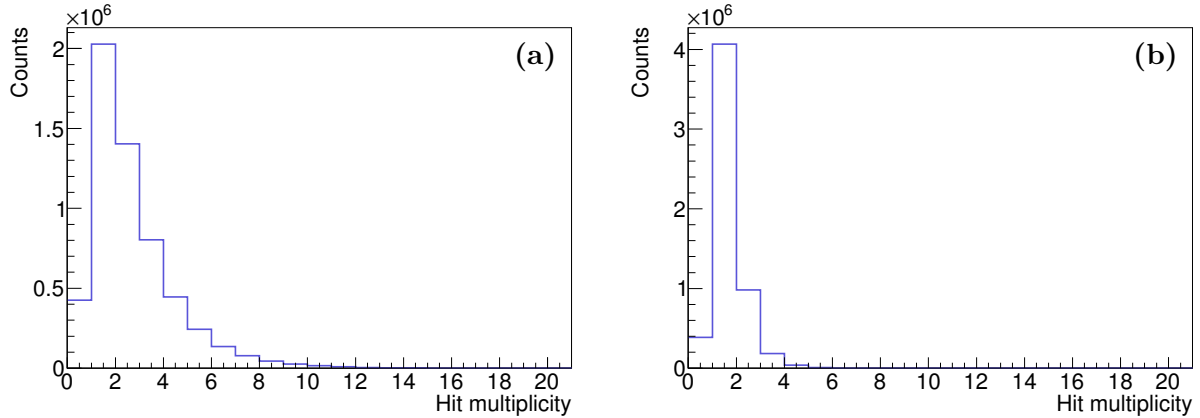
Figure 5.19: Hit multiplicity at a central beam momentum of 1.7 GeV/c with the correlation of front and back plane based also on the time and ADC information **(a)** for the first and **(b)** for the second tracking station.
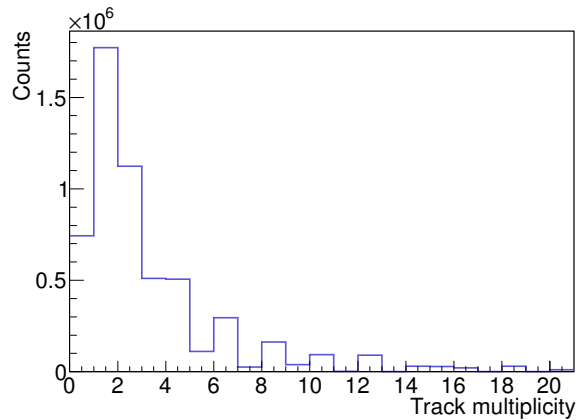
Figure 5.20: Track multiplicity at a central beam momentum of 1.7 GeV/c with a clustering based only on the time, strip number and ADC information.

Considering that just one pion finally reacted with the target material within one LV1 trigger, a selection of the proper track needs to be performed later on for both data sets with the first step (0.690 GeV/c) and both steps (1.7 GeV/c) of the hit correlation applied.

6 Momentum reconstruction

6.1 Beam optics transport code
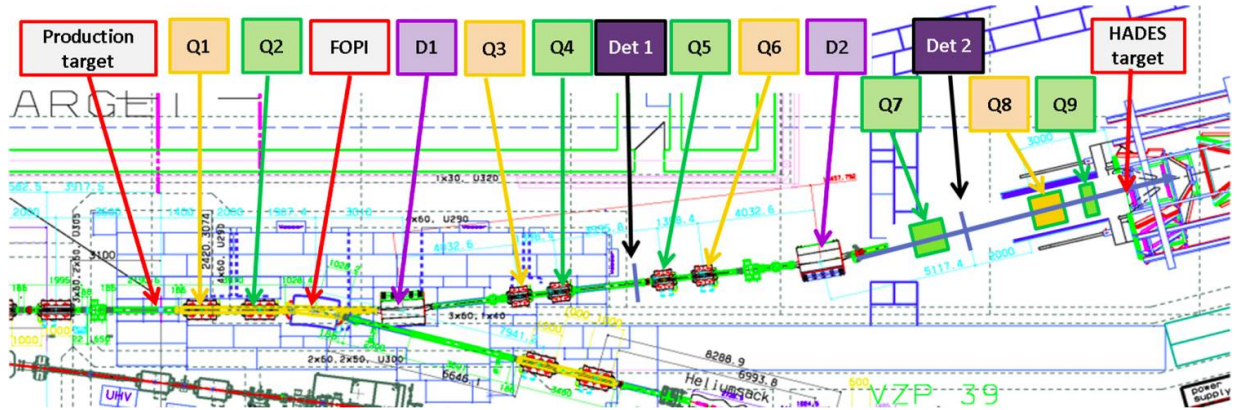
Figure 6.1: Technical drawing of the pion beam chicane, between the pion production target and the HADES cave. All the components (quadrupoles, dipoles and the two tracking stations) are indicated. [Fab13]

In Figure 6.1 the technical drawing of the pion beam chicane is shown. All the components, quadrupoles, dipoles and the two tracking stations, between the pion production target and the HADES cave are indicated. The momentum reconstruction is based on the four spatial coordinates measured by the two tracking stations and the beam optics transport code. Whereas, the beam optics transport code contains the description of the pion beam chicane on the basis of first T_{ij} and second order T_{ijk} coefficients, which carry the information of the geometrical and chromatic aberrations. Since the contribution of the third order effects is small, they are neglected. The properties of the pions at the production target can be calculated using the following formalism:

$$x_i = \sum_{j=1,6} T_{i,j} \cdot x_j + \sum_{j=1,6} \sum_{k=1,6} T_{ijk} \cdot x_j x_k, \tag{6.1}$$

where the following variables x_i ($i = 1,2,3,4,6$) describe the initial condition at the production target:

- x_1: x_0 [cm], the x coordinate at the pion production target
- x_2: θ_0 [mrad], the horizontal angle (definition: $\tan(\theta_0) = \frac{dx}{dz} = \frac{p_x}{p_z}$)
- x_3: y_0 [cm], the y coordinate at the pion production target
- x_4: φ_0 [mrad], the vertical angle $\tan(\varphi_0) = \frac{dy}{dz} = \frac{p_y}{p_z}$)
- x_6: δ [%], the momentum offset in respect to the central beam momentum $\delta = (\frac{p_{rec} - p_{ref}}{p_{ref}})$

Taking only contributions above half of the detector resolution and the four spatial coordinates at the two tracking stations into account, one can calculate the beam properties at the production target with the following equations:

$$X^{det1} = T_{11}^{det1} \cdot x_0 + T_{12}^{det1} \cdot \theta_0 + T_{14}^{det1} \cdot \varphi_0 + T_{16}^{det1} \cdot \delta + T_{116}^{det1} \cdot x_0 \cdot \delta + T_{126}^{det1} \cdot \theta_0 \cdot \delta + T_{146}^{det1} \cdot \varphi_0 \cdot \delta + T_{166}^{det1} \cdot \delta^2$$

$$X^{det2} = T_{11}^{det2} \cdot x_0 + T_{12}^{det2} \cdot \theta_0 + T_{14}^{det2} \cdot \varphi_0 + T_{16}^{det2} \cdot \delta + T_{116}^{det2} \cdot x_0 \cdot \delta + T_{126}^{det2} \cdot \theta_0 \cdot \delta + T_{146}^{det2} \cdot \varphi_0 \cdot \delta + T_{166}^{det2} \cdot \delta^2$$

$$Y^{det1} = T_{32}^{det1} \cdot \theta_0 + T_{33}^{det1} \cdot y_0 + T_{34}^{det1} \cdot \varphi_0 + T_{36}^{det1} \cdot \delta + T_{336}^{det1} \cdot y_0 \cdot \delta + T_{346}^{det1} \cdot \varphi_0 \cdot \delta + T_{366}^{det1} \cdot \delta^2$$

$$Y^{det2} = T_{32}^{det2} \cdot \theta_0 + T_{33}^{det2} \cdot y_0 + T_{34}^{det2} \cdot \varphi_0 + T_{36}^{det2} \cdot \delta + T_{336}^{det2} \cdot y_0 \cdot \delta + T_{346}^{det2} \cdot \varphi_0 \cdot \delta + T_{366}^{det2} \cdot \delta^2$$

$$(6.2)$$

Since the the two dipoles are tilted by 21.75°, the vertical and horizontal plane is coupled leading to the following not negligible coupling terms: $T_{14}, T_{32}, T_{146}, T_{336}, T_{346}, T_{366}$. The four equations (Eq. (6.2)) with five unknown can only be solved by neglecting the smallest impact, which is x_0. Furthermore, these equations have to be solved iteratively, because of the coupling. [Fab13]
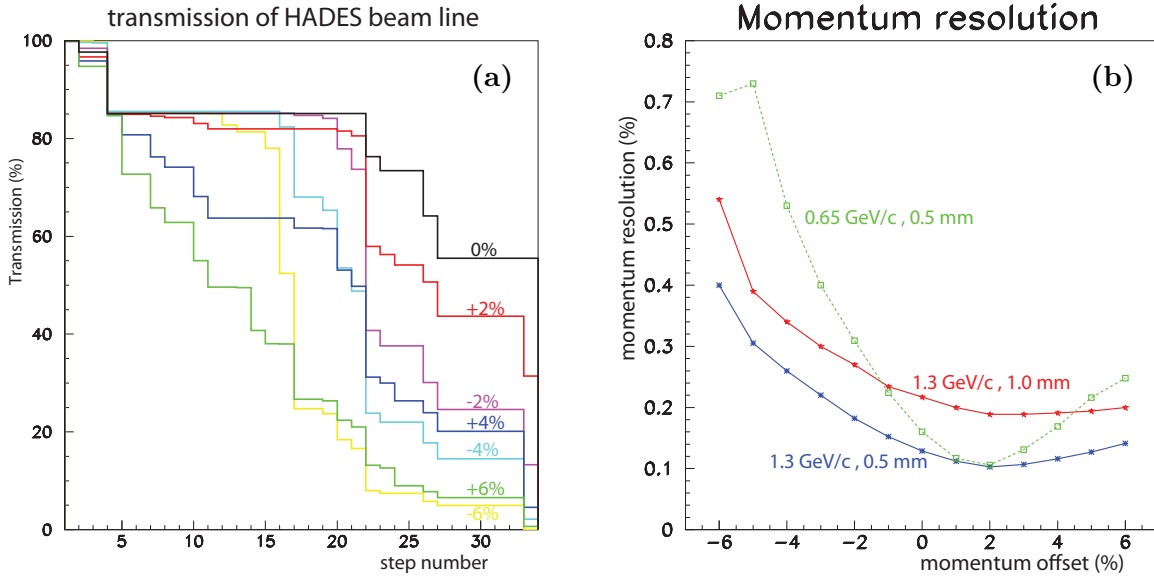
Figure 6.2: **(a)** Transmission of the pion beam chicane based on a Monte Carlo simulation for various momentum offsets ($-6\% \leq \delta \leq +6\%$) as a function of step numbers (Appendix A.1), which indicate the different geometrical acceptances of the quadrupoles and dipoles. The transmission has an asymmetric behaviour comparing positive and negative momentum offsets and completely dies off for huge momentum offsets. [Fab13] **(b)** Pion momentum resolution against the momentum offset δ. The minimal resolution of about 0.1% is constraint by the multiple scattering inside the first detector as well as the position of this detector, which is located in the focal plane of the momentum offset $\delta = +2\%$. [Fab13]

A Monte Carlo simulation was carried out where each pion produced at the production target is traced all along the pion beam chicane within the geometrical acceptance of all the quadrupoles and dipoles. The distribution at the production target was taken to be Gaussian-like in x_0 and y_0 with a rms value of 0.5 mm and a uniform distribution in θ_0 ($\Delta \theta = \pm 10$ mrad), φ_0 ($\Delta \varphi = \pm 50$ mrad) and δ ($\delta = \pm 6\%$). [Fab13]

In Figure 6.2 (a) the transmission of the pion chicane is displayed against step numbers. The step numbers indicate the different geometrical aberrations of the quadrupoles, dipoles and detectors along the way (Appendix A.1). Step number 17 and 26 represent the geometrical size of the first and second silicon sensor, whereas step number 33 corresponds the transmission at the HADES target. At huge momentum offsets ($\delta > +6\,\%$ or $\delta < -6\,\%$) the transmission completely dies off. Moreover, the transmission is asymmetric comparing positive and negative δ. [Fab13]

Since not all momenta focus in the first detector plane, the resolution of the various momenta differ (Fig. 6.2 (b)). The minimal resolution which is constrained by the multiple scattering inside the first detector is achieved for a momentum offset of $\delta = +2\%$. This is due to the fact that the first detector is located in the focal plane. However, the resolution gets significantly worse, the farer one moves away from this momentum offset. [Fab13]

6.2 Momentum calibration

Prior to the actual physics production run with the secondary pion beam the calibration of the reconstructed momentum has been carried out. For this calibration measurement both detector station are installed at their final position (Fig. 6.3). The calibration has been carried out with a proton beam with six different known momenta with respect to the central beam momentum of $2.68\,\mathrm{GeV/c}$ set by the accelerator. In Figure 6.4 one can see that the x-position of the first sensor, which is located close to the dispersive plane, is strongly coupled with the momentum, since the seven different momenta end up at different x-positions. In the end the momentum is evaluated on the basis of the beam optic transport code and the four position information delivered by the pion tracker. All seven different reconstructed momenta can be clearly distinguished and are in good agreement with the reference values (Fig. 6.5). There is only a slight shift in the low momentum region. Since not all the momenta focus in the first detector plane the resolution of the various reconstructed momenta differ. But all the resolutions are below the requested one of 0.5%. Table 6.1 summarizes the results.
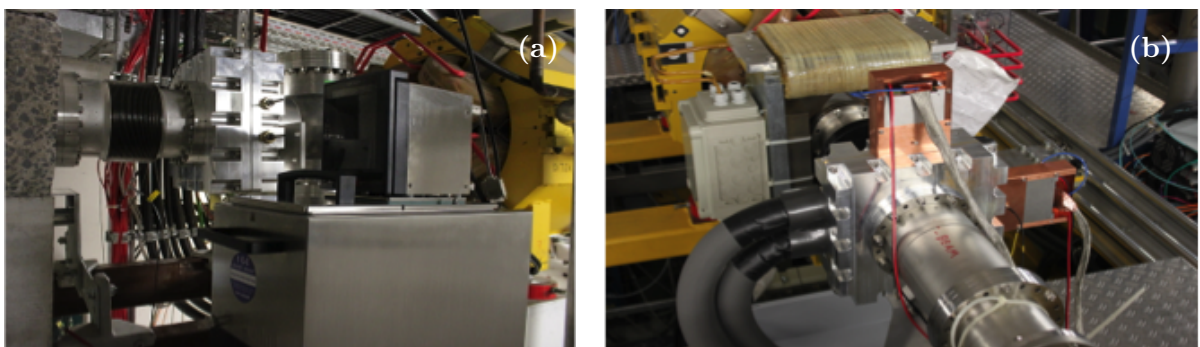
Figure 6.3: Photographs of the two tracking stations installed along the pion beam chicane at their final positions **(a)** in the NE5 area and **(b)** in the Hades cave.
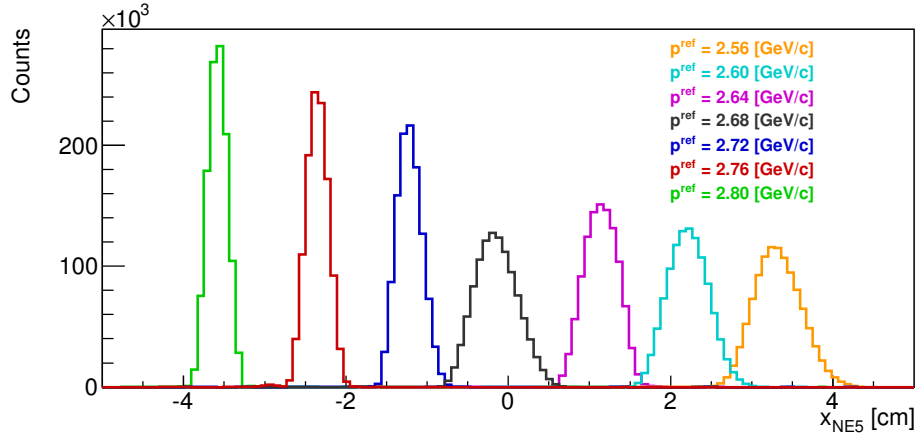
Figure 6.4: Measured x-position of the first tracking station located in the NE5 area. The different colors indicate the different momenta.
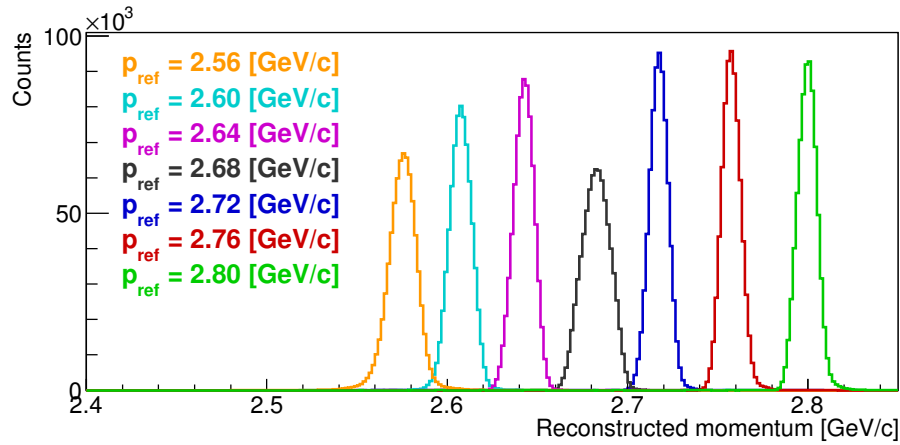
Figure 6.5: Reconstructed momentum calibration performed with six known momenta with respect to the central beam momentum of 2.68 GeV/c, set by the accelerator.

RefMom [GeV/c]	RecMom [GeV/c]	Resolution [%]
2.56	2.58	0.29
2.60	2.61	0.24
2.64	2.64	0.21
2.68	2.68	0.27
2.72	2.72	0.19
2.76	2.76	0.18
2.80	2.80	0.19

Table 6.1: Values of the reconstructed proton momentum compared to the reference values, set by the accelerator, as well as the momentum resolutions obtained with CERBEROS.

6.3 Reconstructed pion momentum

In Figure 6.6 the distribution of the reconstructed pion momentum for all possible combinations of the hits in the first and second tracking station is depicted. The maximum transmission occurs exactly at the central beam momentum of $1.7\,\mathrm{GeV/c}$, since the beam maximum is nicely centred in the middle of the x-layer of the first tracking station (Fig. 5.4 (a)), which is located close to the dispersive plane. Nevertheless, by comparing the distribution to the one obtained with a selected sample containing events with only one hit in all four layers, one can see that this distribution is much too broad. Furthermore, by considering that just one pion finally reacted with the target material within one LV1 trigger, a selection of the proper track, hence the proper reconstructed momentum, has to be applied.
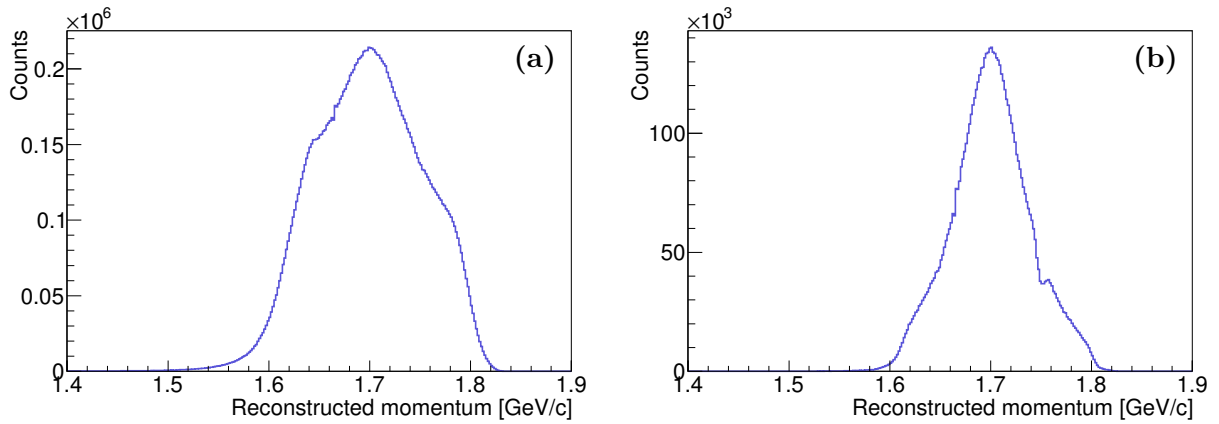
Figure 6.6: Distribution of the reconstructed momentum at a central beam momentum of $1.7\,\mathrm{GeV/c}$ **(a)** for all possible track combination **(b)** for event with only one track in all four layers.

The selection is based on the correlation of the y-position of the first and second tracking station (Fig. 6.7 (a)). The correlation is scanned in y-slices and the distribution of each slices is fitted with a Gaussian. The obtained mean value for each slice is then plotted and at the end fitted with a linear function, which is depicted in Fig. 6.7 (b). The obtained slope and offset is then used for the selection. Thereby, the track with the smallest distance to the slope is selected in each event. The pion momentum distribution after this selection, which reproduces the shape of distribution of the purified sample, is displayed in Fig. 6.8. Moreover, it shows an asymmetry of lower and higher momenta compared to the central beam momentum as expected by the simulations (Fig. 6.2 (a)).

Figure 6.9 depicts the distribution of the reconstructed pion momentum for all possible combinations of the multiple hits in the first and second tracking station. The maximum transmission occurs not at the central beam momentum of $0.690\,\mathrm{GeV/c}$, but is shifted to $0.698\,\mathrm{GeV/c}$, since the beam maximum was shifted to lower strip numbers (Fig. 5.5 (a), Appendix A.2) corresponding to negative x-positions (Eq. (5.1)), on the x-layer of the first tracking station, which is located close to the dispersive plane (Fig. 6.4, Fig. 6.5). In addition, by comparing this distribution to the one obtained with a purified sample containing only events with just one selected track candidate, one can see that this distribution is also much broader. Therefore, also in this case a selection of the proper track has to be applied.
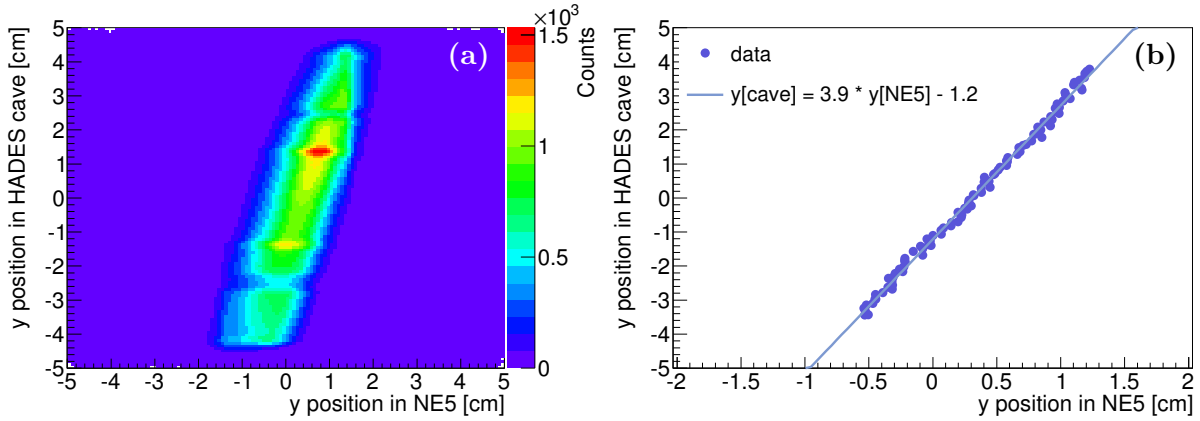
Figure 6.7: (a) Correlation of the y-position of the first and second sensor for events with only one track (1.7 GeV/c). **(b)** Extracted slope based on the correlation of the y-position of the first and second sensor.
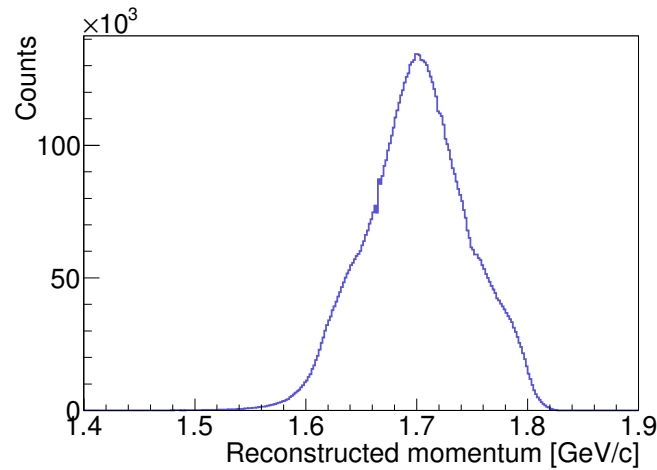
Figure 6.8: Distribution of the reconstructed momentum at a central beam momentum of 1.7 GeV/c, in which the selection on the yy-correlation is applied.

Since in this data sample, the hit-finder is only relying on the time and strip information, the sample is contaminated by ambiguities, wrong combinations of the x- and y-positions as well as combinations of real hits with noise or two hits originating from noise, as explained in Section 5.5.1. Considering that the x-position of the first tracking station, close to the dispersive plane, has a huge influence on the reconstructed momentum (Fig. 6.4,), a selection based on the correlation of the y-position of the first and second sensor (Fig. 6.10 (a)) is not sufficient. Therefore, another selection method has to be implemented. Since during this physics production run a polyethylene target was employed, the selection procedure is cross-checked with elastic scattering events $(\pi^- + p)$, which will be explained in detail in the next section.
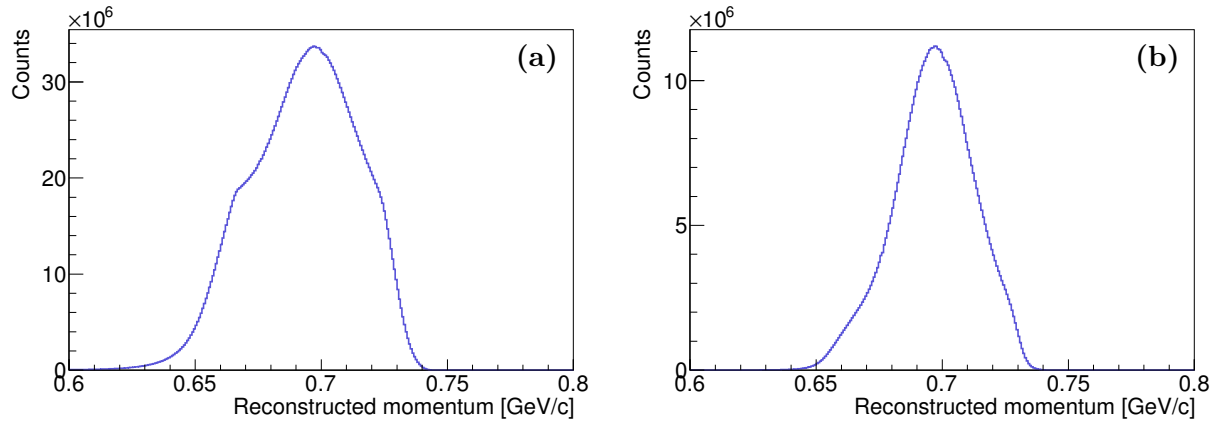
Figure 6.9: Distribution of the reconstructed momentum at a central beam momentum of $0.690\,\mathrm{GeV/c}$ **(a)** for all possible track combinations **(b)** for events with only one track in all four layers.
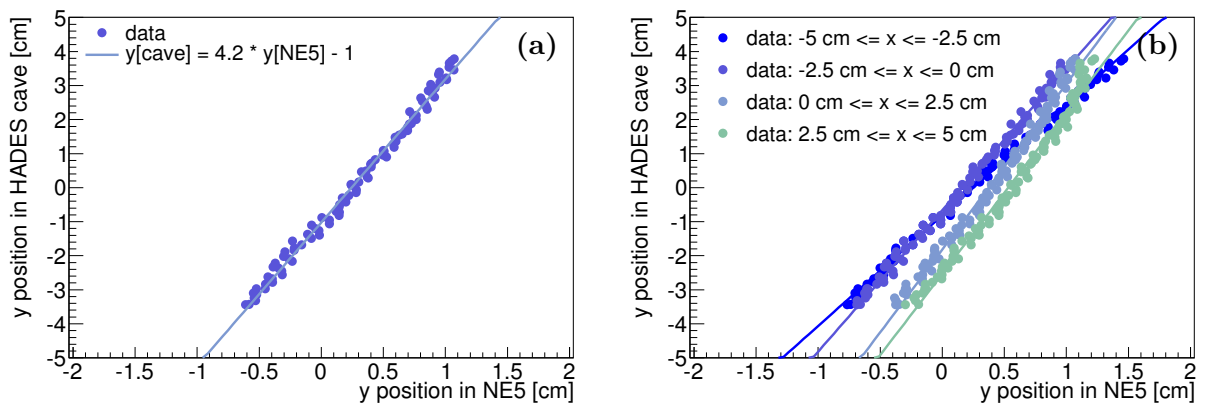
Figure 6.10: **(a)** Extracted slope based on the correlation of the y-position of the first and second sensor for events with only one track ($0.690\,\mathrm{GeV/c}$). **(b)** Extracted slopes based on the y-position correlation in the different x-position regions on the first sensor.

6.4 Elastic scattering

One way to cross-check the reconstructed pion momentum is the study of elastic events:
$\pi^- + p \to \pi^- + p$.
These physical events originating from elastic scattering can be reconstructed exclusively due to momentum and energy conservation and therefore should give rise to the momentum of the impinging pions on the polyethylene target (H_4C_2). By applying the invariant mass technique, which is commonly used in the investigation of short lived particles that decay before reaching the detectors, one can reconstruct the total available energy of the elastic process.

The invariant mass (M) is the sum of the four-vectors ($E_i, \vec{p_i}$), where momentum of the particle ($\vec{p_i}$) is reconstructed in HADES on the basis of the deflection of particle trajectories while traversing a magnetic field according to the Lorentz force. In detail the momentum ($\vec{p_i}$) is determined by the bending radius extracted from the positions measured by the two layers MDC in front and after the magnet. After the particle identification (PID) the energy of the particle (E_i) is calculated with $E_i = \sqrt{m_i^2 c^4 + p_i^2 c^2}$.

For the elastic scattering events the invariant mass ($M_{\pi^- p}$) is calculated the following way (n = number of partciles = 2):

$$
\begin{aligned}
M_{\pi^- p} &= \frac{1}{c^2}\sqrt{E^2 - (\vec{p})^2 c^2} = \frac{1}{c^2}\sqrt{\left(\sum_{i=1}^{n} E_i\right)^2 - \left(\sum_{i=1}^{n} \vec{p_i}\right)^2 c^2} \\
&= \frac{1}{c^2}\sqrt{\left(E_{\pi^-}^* + E_p^*\right)^2 - \left(\vec{p^*}_{\pi^-} + \vec{p^*}_p\right)^2 c^2} \\
&= \sqrt{m_{\pi^-}^2 + m_p^2 + 2\left(\frac{1}{c^4} E_{\pi^-}^* E_p^* - \frac{1}{c^2}\vec{p^*}_{\pi^-}\vec{p^*}_p\right)}
\end{aligned}
\tag{6.3}
$$

This reconstructed total available energy ($M_{\pi^- p}$) should be equal to the Center-of-Mass energy $\sqrt{s}$ calculated with the reconstructed pion momentum p_{π^-} assuming the protons at rest in the following way:

$$
\begin{aligned}
\sqrt{s} &= \sqrt{\left(\sum_i^n P_i\right)^2} = \sqrt{(P_{\pi^-} + P_p)^2} \\
&= \sqrt{P_{\pi^-}^2 + 2P_{\pi^-}P_p + P_p^2} = \sqrt{2\frac{1}{c^2}E_{\pi^-}m_p + m_{\pi^-}^2 + m_p^2},
\end{aligned}
\tag{6.4}
$$

with $E_{\pi^-} = \sqrt{m_{\pi^-}^2 c^4 + p_{\pi^-}^2 c^2}$.

6.4.1 Elastic scattering theory
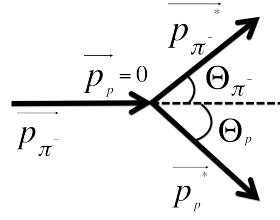
Figure 6.11: Schematic of a elastic scattering event $(\pi^- + p \to \pi^- + p)$ in the laboratory frame.

In the case of elastic scattering events, no new particle is produced, the beam particle (P_{π^-}) is impinging on the target particle (P_p) where the pion and proton in the final state are detected in the HADES detector systems.

$$P_{\pi^-} + P_p = P_{\pi^-}^* + P_p^* \tag{6.5}$$

These two particles in the final state lead to 8 kinematic degrees of freedom represented by the two 4-vectors $(P_{\pi^-}^*, P_p^*)$. Two components are fixed by the masses of the particle. Three others are fixed by the momentum conservation:

$$0 = p_{\pi^-,x}^* + p_{p,x}^*$$
$$0 = p_{\pi^-,y}^* + p_{p,y}^*$$
$$p_{\pi^-,z} = p_{\pi^-,z}^* + p_{p,z}^* \tag{6.6}$$

And finally one is fixed by the energy conservation:

$$\sqrt{p_{\pi^-,z}^2 c^2 + m_{\pi^-}^2 c^4} + m_p = \sqrt{(p_{\pi^-,x}^{*2} + p_{\pi^-,y}^{*2} + p_{\pi^-,z}^{*2})c^2 + m_{\pi^-}^2 c^4} + \sqrt{(p_{p,x}^{*2} + p_{p,y}^{*2} + p_{p,z}^{*2})c^2 + m_p^2 c^4} \tag{6.7}$$

All the components of the 4-vectors can be deduced by measuring two observables, the two remaining degrees of freedom.
Whereas the scattering angles are defined the following way:

$$\theta_{\pi^-} = \arccos\left(\frac{p_{\pi^-,z}^*}{|\vec{p}_{\pi^-}^*|}\right)$$

$$\theta_p = \arccos\left(\frac{p_{p,z}^*}{|\vec{p}_p^*|}\right)$$

$$\varphi_{\pi^-} = \arctan\left(\frac{p_{\pi^-,x}^*}{p_{\pi^-,y}^*}\right)$$

$$\varphi_p = \arctan\left(\frac{p_{p,x}^*}{p_{p,y}^*}\right) \tag{6.8}$$

For the elastic channel, the azimuthal angle of the pion (φ_{π^-}), differs by exactly 180° from the azimuthal angle of the proton (φ_p) due to momentum conservation (Eq. (6.6)).

6.4.2 Selection of elastic scattering events

First of all the pions and protons detected in the HADES detector systems must be identified. The particle identification (PID) can be performed using the specific energy loss dE/dx (Eq. (3.1)) information together with the momentum p or the velocity β together with momentum p, since in the case of the β there is the following relation:

$$p = c\beta\gamma m = mc\frac{\beta}{\sqrt{1-\beta^2}} \tag{6.9}$$

The velocity β of the particle can be calculated with the help of the travelled path length l_{META} from the event vertex in the META detectors and the time-of-flight (tof) measurements, achieved with the Start detector and the TOF/RPC detectors: $\beta = l_{META}/tof$.
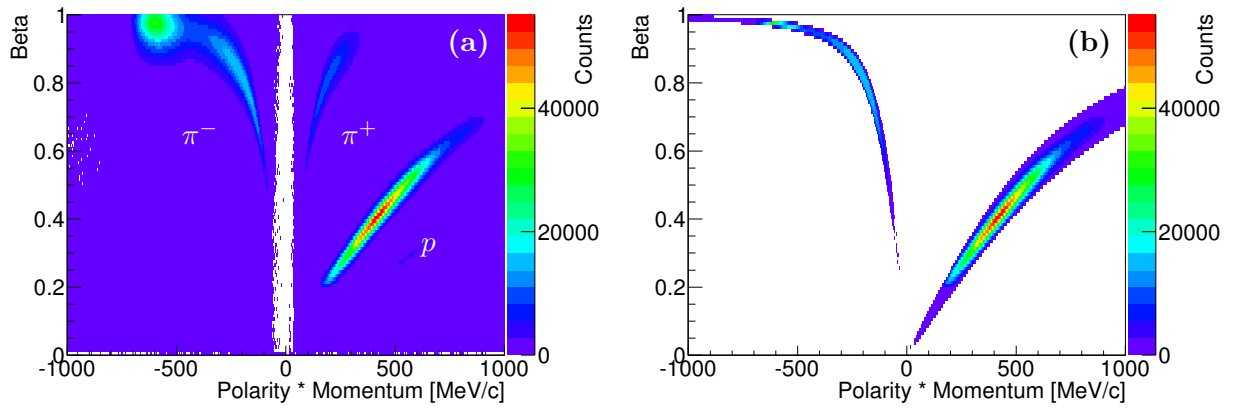
Figure 6.12: Beta vs. momentum times charge **(a)** for all detected particles and **(b)** for the π^- and p after the particle identification.
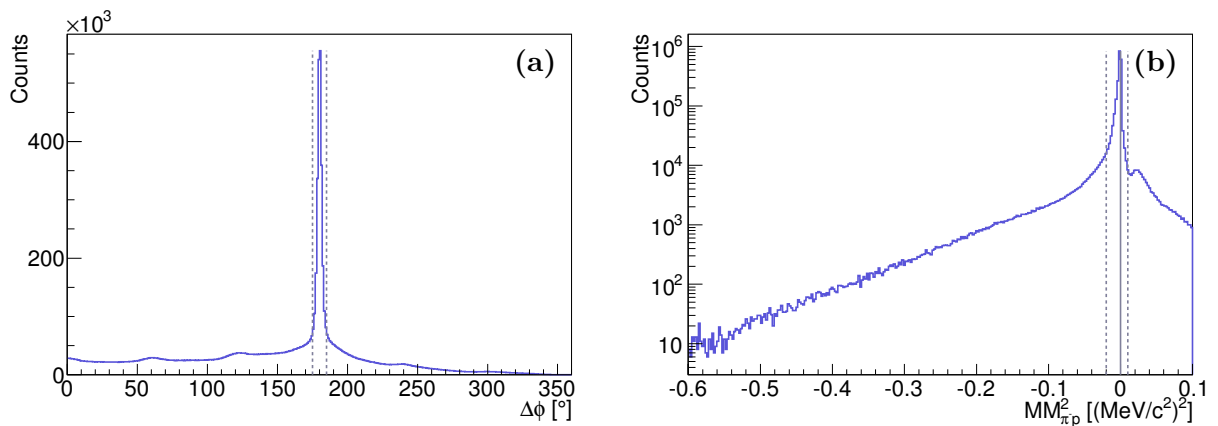
Figure 6.13: **(a)** Distribution of the difference of the azimuthal angle of the pion and proton. **(b)** Squared missing mass spectrum for the pion and proton detected in the HADES spectrometer with an applied coplanarity cut.

Therefore, the velocity β as a function of momentum p should differ, due to the different masses of the different particle species and thus can be used for the PID. In Figure 6.12 (a) beta as a function of momentum times charge is depicted. One the left-hand side of the plot negatively charged particles are observed dominated by π^-, whereas on the right-hand side π^+ and p are visible. Figure 6.12 (b) pictures the π^- and p after the applied particle identification for the further analysis. The elastically scattered pions cover a momentum region of $350\,\text{MeV/c} < p_{\pi^-} < 700\,\text{MeV/c}$ and since a very strict PID cut is applied, only a small amount of pions is selected leading to reduce sample. But still the full momentum region is covered.

The elastic scattering events are selected on the basis of the momentum conservation with a coplanarity cut of $175° < | \varphi_{\pi^-} - \varphi_p | < 185°$ (Fig. 6.13 (a)). Moreover, the sample can be purified with an additional cut on the missing mass, since in the case of elastic scattering no additional particle is produced and therefore, the missing mass should be centred around zero. The missing mass (MM_{π^-p}) is defined in the following way (n = number of partciles = 2):

$$
\begin{aligned}
MM_{\pi^-p} &= \frac{1}{c^2} \sqrt{\left(E_b + E_t - \sum_i^n E_i\right)^2 - \left(\vec{p}_b + \vec{p}_t - \sum_i^n \vec{p}_i\right)^2 c^2} \\
&= \frac{1}{c^2} \sqrt{\left(E_{\pi^-} + E_p - E_{\pi^-}^* - E_p^*\right)^2 - \left(\vec{p}_{\pi^-} + \vec{p}_p - \vec{p^*}_{\pi^-} - \vec{p^*}_p\right)^2 c^2},
\end{aligned}
\tag{6.10}
$$

where $(E_b, \vec{p_b})/(E_{\pi^-}, \vec{p_{\pi^-}})$ and $(E_t, \vec{p_t})/(E_p, \vec{p_p})$ are the 4-momenta of the beam and target particle, respectively.

The squared missing mass distribution ($MM_{\pi^-p}^2$) of the π^-p-system is depicted in Fig. 6.13 (b) calculated for a pion momentum of $0.698\,\text{MeV/c}$ corresponding to the value at the maximum transmission (Fig. 6.9 (b)). The peak of the elastic scattering events is not centred around zero, but shifted to lower values. By applying a cut around the region of the elastic events ranging from $-0.02\,(\text{MeV/c}^2)^2 < MM^2 < 0.01\,(\text{MeV/c}^2)^2$, the sample is purified furtheron. Especially in terms of the contamination of events originating from $\pi^- + C$ in the employed polyethylene target (H_4C_2) leading to a broadening of the missing mass peak, due to the Fermi motion.
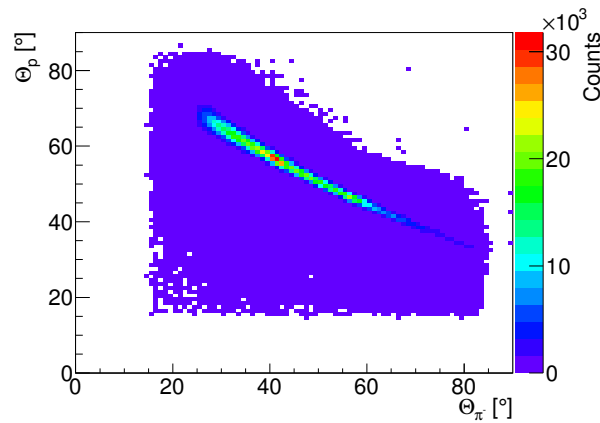
Figure 6.14: Correlation between the two scattering angles, Θ_{π^-} and Θ_p with an applied cut on the missing mass spectrum ($-0.02\,(\text{MeV/c}^2)^2 < MM^2 < 0.01\,(\text{MeV/c}^2)^2$) as well as on the coplanarity.
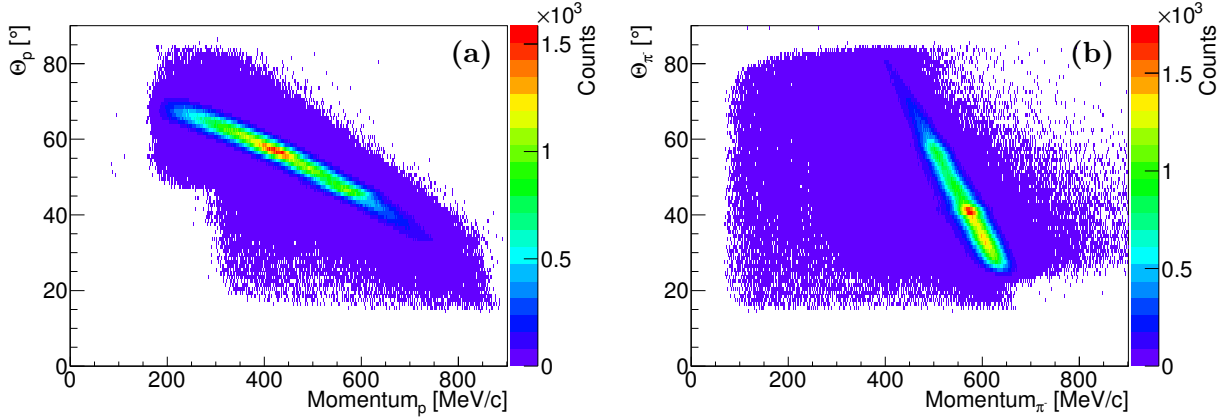
Figure 6.15: Correlation of **(a)** the momentum and scattering angle (Θ_p) for the proton and **(b)** the momentum and the scattering angle (Θ_{π^-}) for the pion with an applied cut on the missing mass distribution (-0.02 (MeV/c^2)^2 < MM^2 < 0.01 (MeV/c^2)^2) as well as on the coplanarity.
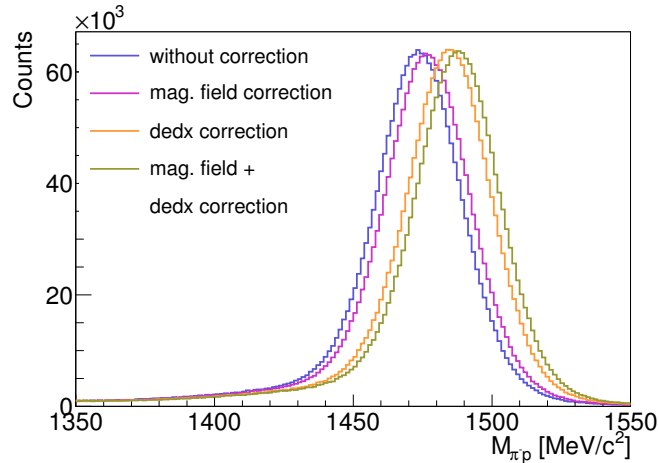
Figure 6.16: Comparison of the invariant mass spectrum for π^- and p detected in HADES with an applied cut on the missing mass spectrum (-0.02 (MeV/c^2)^2 < MM^2 < 0.01 (MeV/c^2)^2) as well as on the coplanarity without correction (blue curve), with the magnetic field correction (pink curve), with the energy loss correction (orange curve) and with the magnetic field and energy loss correction (green curve).

As expected, the two scattering angles (Θ_{π^-}, Θ_p) as well as the scattering angle and the momentum for each particle, proton and pion, are nicely correlated (Fig. 6.14, Fig. 6.15 (a), (b)). The invariant mass distribution of the $\pi^- p$-system is depicted in Fig. 6.16 (blue curve) with a mean value of 1474 MeV/c^2 and a resolution of 1.1 % originating from the resolution obtained with the HADES detector systems as well as due to the broad momentum distribution of the impacting pions. Additionally, one can apply a correction of the magnetic field with an upscale of the momenta reconstructed with HADES by 1.006. This correction is empirical originating from the fact that the TOSCA field map was stretched from room temperature to liquid helium temperatures by making assumptions on the expansion of the coil [Mak15]. The upscale leads to a shift of the mean value to 1477 MeV/c^2 (Fig. 6.16 pink curve). Besides, a correction of reconstructed momentum for

each, pion and proton, in terms of the energy loss in the region between the target and the MDC II chambers can be applied, leading to a mean value of $1484\,\mathrm{MeV/c^2}$ (Fig. 6.16 orange curve). By applying both momentum corrections simultaneously even a mean value of $1488\,\mathrm{MeV/c^2}$ is reached (Fig. 6.16 green curve). For the further analysis the invariant mass spectrum obtained after the magnetic field and energy loss correction is taken into account, but nevertheless a more accurate investigation of the all the corrections is required in future.

	without	mag. field	dedx	mag. field + dedx
Invmass [MeV/c²]	1474	1477	1484	1488

Table 6.2: Comparison of the mean values of the invariant mass distribution of the $\pi^- p$-system obtained without any corrections and after applying different corrections.

6.4.3 Selection of the reconstructed pion beam momentum

Since the $\sqrt{s}$ is calculated on the basis of the reconstructed beam momentum, the selection procedure of the momentum has to be applied before comparing the invariant mass distribution with the obtained $\sqrt{s}$ distribution. Therefore, two different selection methods are investigated with respect to the reference distribution including only events with one beam track candidate. The first method is just based on the correlation of the y-position on the first and second tracking stations (Fig. 6.10 (a), (b)) like the selection method for the reconstructed momentum at a central beam momentum of $1.7\,\mathrm{GeV/c}$:

$$r_{yy} = \left| \frac{-4.2 * y_{NE5} + y_{HADES} - 1}{\sqrt{4.2^2 + 1}} \right| \tag{6.11}$$

Hence, the track candidate with the smallest distance ($r_{yy} \to min$) is selected for further analysis. As explained in Section 6.3, a selection only on this yy-correlation is not sufficient, since the influence on the x-position is only small. For this reason, this selection method is used only as a reference for the second one. The second method is based on the yy-correlation as well as on the different transmission losses of the various momentum offsets with respect to the central beam momentum shown in Fig. 6.2 (a). Since the maximum transmission occurs not at the central beam momentum, but is shifted to higher values, the value with the maximum transmission obtained with the pure sample containing only one beam track is used. In the case of the $0.690\,\mathrm{GeV/c}$ the maximum transmission occurs at $0.698\,\mathrm{GeV/c}$ ($MaxMom$) (Fig. 6.9 (b)). Therefore, the selection is based on the following equation:

$$r_{both} = \sqrt{100000 * \left(\frac{-4.2 * y_{NE5} + y_{HADES} - 1}{\sqrt{4.2^2 + 1}} \right)^2 + (MaxMom - RecMom)^2} \tag{6.12}$$

A weighting factor of 100000 is introduced to enhance the yy-correlation dependence and therefore, to keep the biasing of the data as minimal as possible, since the selection is also based on the distance of the reconstructed value with respect to the one at the maximum transmission. Again the reconstructed momentum with the smallest distance ($r_{both} \to min$) is selected. All

the three different reconstructed momentum distributions are depicted in Fig. 6.17 (a). The distribution indicated in dark blue corresponds to the reference sample containing almost no ambiguities. The other ones represent the two different selection methods based on the yy-correlation (first selection method/*yy selection*: light blue curve) or on the yy-correlation and the maximum transmission (second selection method/*both selection*: medium blue curve), whereas the distribution of both selection methods are scaled down to be comparable to the reference sample. Both selection methods lead to a shift to higher momenta with a value of $0.701\,\mathrm{GeV/c}$ at the maximum transmission for the first selection method and $0.700\,\mathrm{GeV/c}$ for the second selection method. Besides, the second selection method reproduces the shape of the reference sample much better.
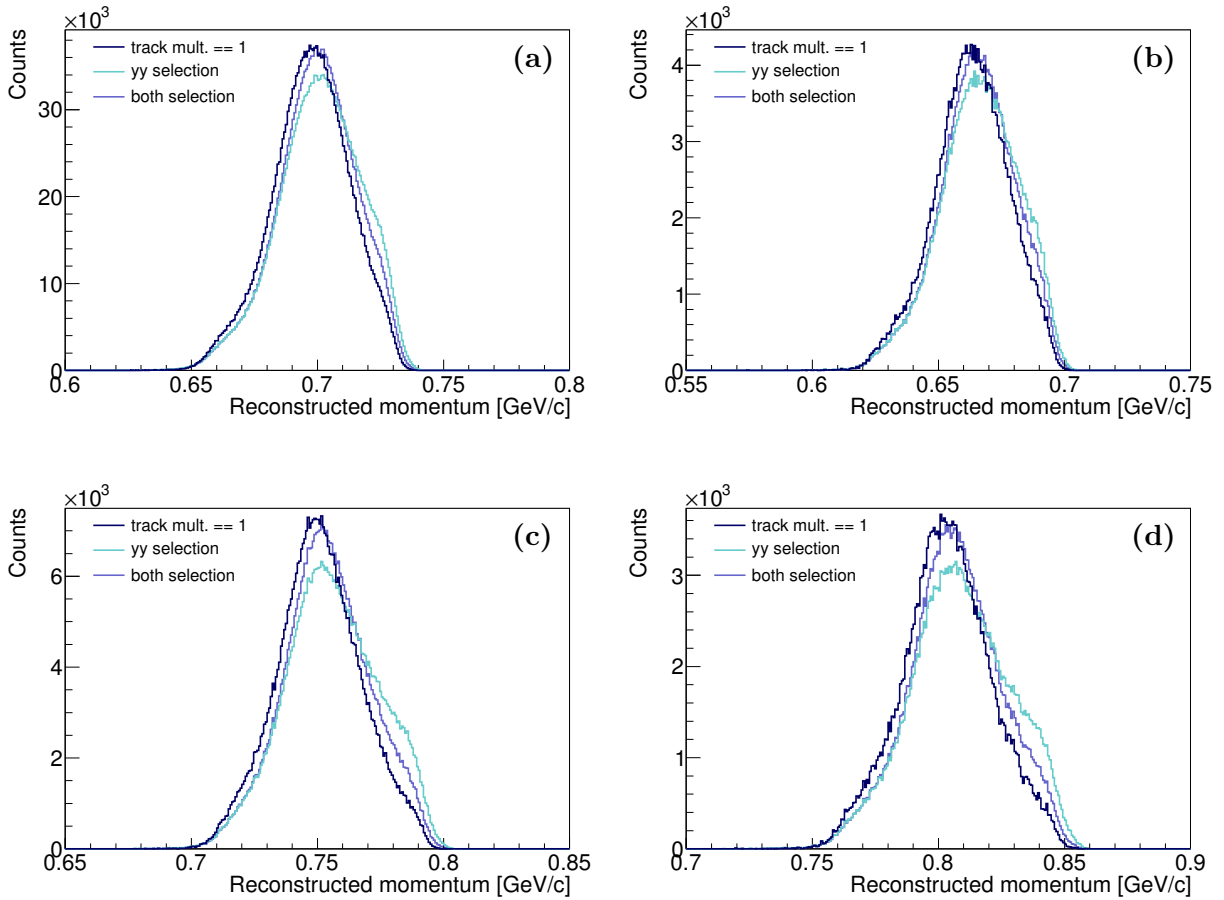
Figure 6.17: Comparison between the momentum distribution of the reference sample ($trackmult. == 1$: dark blue curve) and both selection methods (*yy selection*: light blue curve, *both selection*: medium blue curve) at a central beam momentum of **(a)** $0.690\,\mathrm{GeV/c}$ **(b)** $0.656\,\mathrm{GeV/c}$ **(c)** $0.748\,\mathrm{GeV/c}$ **(d)** $0.800\,\mathrm{GeV/c}$.

The reconstructed momentum distributions obtained at the several central beam momenta ($0.656\,\mathrm{GeV/c}$, $0.748\,\mathrm{GeV/c}$, $0.800\,\mathrm{GeV/c}$) are pictured in Fig. 6.17 (b), (c), (d). In Table 6.3 the mean values for the reference sample as well as for both selection methods are listed for the several central beam momenta. The shift of the maximum transmission originated from a shift on the x-layer of the first tacking station differs comparing all different central beam momenta. Whereas,

for the data obtained at $0.748\,\text{GeV/c}$ only a slight shift occurs with a maximum transmission at $0.750\,\text{GeV/c}$. All in all no trend is visible by comparing the different central beam values, since the shift with a value of $0.004\,\text{GeV/c}$ for the data accomplished at $0.800\,\text{GeV/c}$ increases again. In all cases the second selection method shifts the maximum transmission to higher values, although in all cases the shape of the reference distribution is much better reproduced by the second selection method, which is even better visible at the higher central beam momenta.

	reference [GeV/c]	yy selection [GeV/c]	both selection [GeV/c]
$0.690\,\text{GeV/c}$	0.698	0.701	0.700
$0.656\,\text{GeV/c}$	0.664	0.667	0.666
$0.748\,\text{GeV/c}$	0.750	0.753	0.753
$0.800\,\text{GeV/c}$	0.804	0.807	0.806

Table 6.3: Comparison of the mean values of the reconstructed momentum obtained with different selection methods at the several central beam momenta.

6.4.4 Comparison between invariant mass and $\sqrt{s}$

After the selection of the reconstructed pion momentum with CERBEROS, the invariant mass distribution is compared to the reconstructed momentum as well as to the obtained $\sqrt{s}$ distribution. In Figure 6.18 (a) the correlation between the invariant mass and the reconstructed momentum selected based on the yy-correlation is depicted. As expected a linear dependence is visible. Since, smaller pion momenta lead to lower available energies ($\sqrt{s}$) and therefore, to lower invariant masses. However, in the high momentum region a broader distribution is observed due to the shoulder of the momentum distribution in this region (Fig. 6.17 (a), light blue curve). This is not the case in Fig. 6.18 (b), which based on the second selection method. By comparing the obtained $\sqrt{s}$ on the basis of this selection with the invariant mass distribution (Fig. 6.19), one observes also an inclination, but besides also a shift of the invariant mass to lower values.
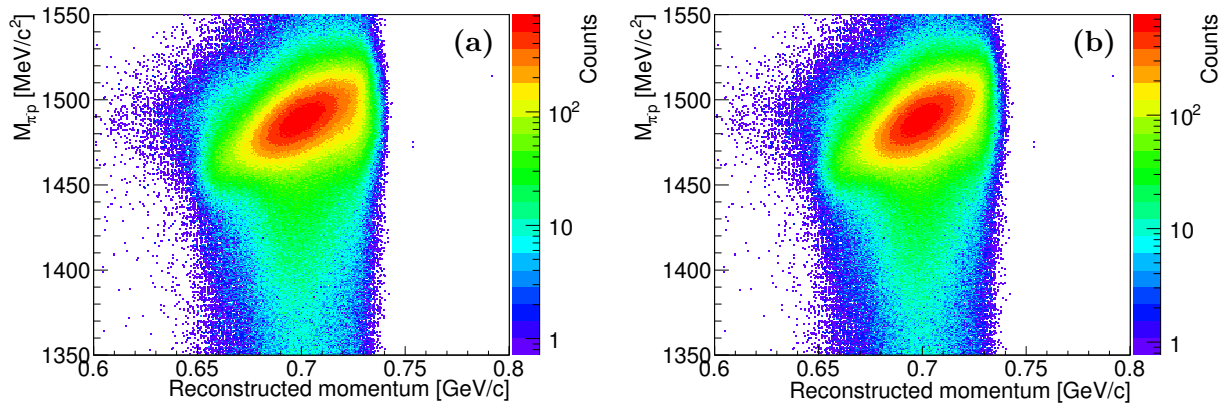
Figure 6.18: Invariant mass distribution for π^- and p detected in HADES (coplanarity cut and -0.02 $(\text{MeV/c}^2)^2 < MM^2 < 0.01\ (\text{MeV/c}^2)^2)$ vs. the reconstructed pion momentum selected on the basis of **(a)** the yy-correlation and **(b)** the yy-correlation as well as the maximum transmission.
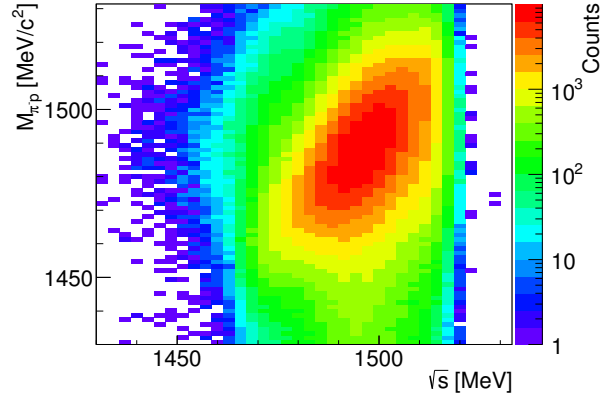
Figure 6.19: Invariant mass spectrum for π^- and p detected in HADES (coplanarity cut and -0.02 $(\mathrm{MeV/c^2})^2 < MM^2 < 0.01\ (\mathrm{MeV/c^2})^2)$ vs. $\sqrt{s}$ calculated with the reconstructed momentum selected with the second method.
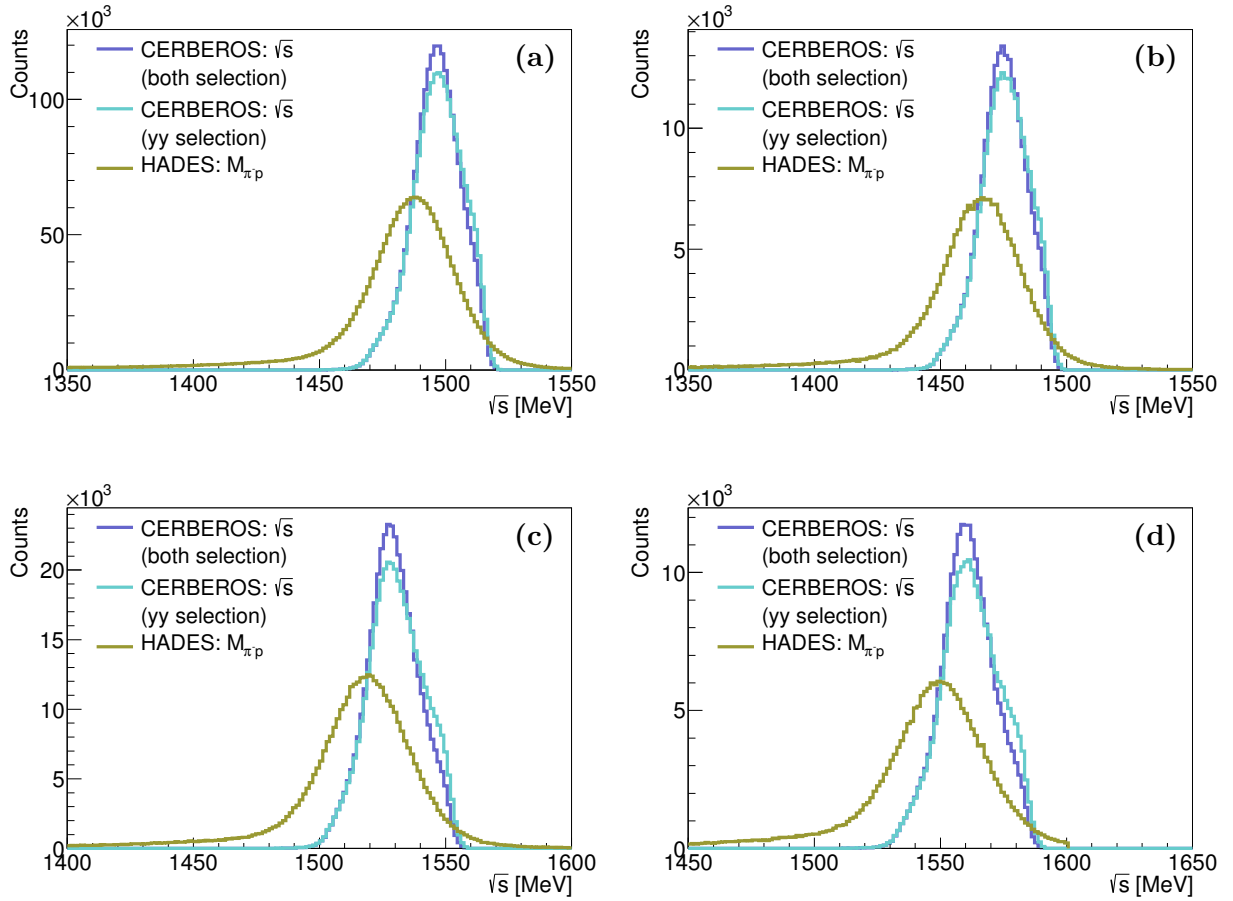
Figure 6.20: Comparison of the π^-p invariant mass (green curve) and the $\sqrt{s}$ calculated with the reconstructed momentum of the secondary pions based on both selection methods (*yy selection*: light blue curve, *both selection*: medium blue curve) at a central beam momentum of **(a)** 0.690 GeV/c **(b)** 0.656 GeV/c **(c)** 0.748 GeV/c **(d)** 0.800 GeV/c.

This shift is even better visible in Fig. 6.20 (a). The green curve indicates the invariant mass distribution, whereas the light blue curve indicates the selection based on the yy-correlation (*yy selection*) and the medium blue curve the selection based on the yy-correlation as well as on the maximum transmission (*both selection*). Here, the $\sqrt{s}$ distributions for both selection methods differ mainly in the region of the mean value. Since the $\sqrt{s_{rec}}$ distribution calculated with the reconstructed momentum obtained on the basis of the second selection method, reproduces the shape of the reference momentum distribution much better, this distribution is compared in detail to the invariant mass distribution. Due to the shift of the maximum transmission to 0.698 GeV/c at a central beam momentum of 0.690 GeV/c, a shift of 8 MeV is observed comparing the $\sqrt{s_{ref}} = 1.489$ GeV (0.690 GeV/c) to $\sqrt{s_{rec}} = 1.497$ GeV (0.698 GeV/c). However, the resolution of the $\sqrt{s_{rec}}$ distribution is smaller compared to the one of the invariant mass, since the resolution obtained with CERBEROS is better than the one obtained with HADES. Nevertheless, a shift of about 9 GeV is observed.

Furthermore, the $\sqrt{s_{ref}}$ and invariant mass distributions obtained at the several central beam momenta (0.656 GeV/c, 0.748 GeV/c, 0.800 GeV/c) are depicted in Fig. 6.20 (b), (c), (d), whereas the mean values of the $\sqrt{s_{ref}}$, $\sqrt{s_{rec}}$ as well as the invariant mass are listed in Table 6.4 for the several central beam momenta. Also in all three other cases a shift of the invariant mass to lower values compared to the $\sqrt{s_{rec}}$ values is observed ranging from $8 \text{ MeV} < \Delta(\sqrt{s_{rec}} - InvMass) < 12 \text{ MeV}$.

	0.690 [GeV]	**0.656** [GeV]	**0.748** [GeV]	**0.800** [GeV]
$\sqrt{s_{ref}}$ [GeV]	1.489	1.468	1.526	1.556
$\sqrt{s_{rec}}$ [GeV]	1.497	1.475	1.529	1.562
$InvMass$ [GeV]	1.488	1.467	1.519	1.550
$\Delta(\sqrt{s_{ref}} - \sqrt{s_{rec}})$ [MeV]	8	7	3	6
$\Delta(\sqrt{s_{rec}} - InvMass)$ [MeV]	9	8	10	12

Table 6.4: Comparison of the mean values of the $\sqrt{s}$ obtained with the reference value ($\sqrt{s_{ref}}$) and the value obtained with the second selection method ($\sqrt{s_{rec}}$) as well as of the invariant mass at the several central beam momenta.

6.4.5 Energy loss simulation of the pion and proton in the target

A part of $\Delta(\sqrt{s_{rec}} - InvMass)$ is originating from the energy loss of the pions and protons inside the polyethylene target and has been investigated with a simplified simulation based on GEANT4 [GEA]. A full scale simulation of the elastic reactions and reconstruction inside the HADES spectrometer should be carried out in the future to evaluate this in more detail. Furthermore, the impact of this energy loss on the invariant mass distribution is examined.

GEANT4 is a flexible toolkit to simulated the interaction of particles with matter covering energy ranges from $250\,\mathrm{eV}$ to $1\,\mathrm{TeV}$. It is an object-oriented toolkit written in C++ based on Monte Carlo simulation including various set of physics models, that are represented by large data libraries.
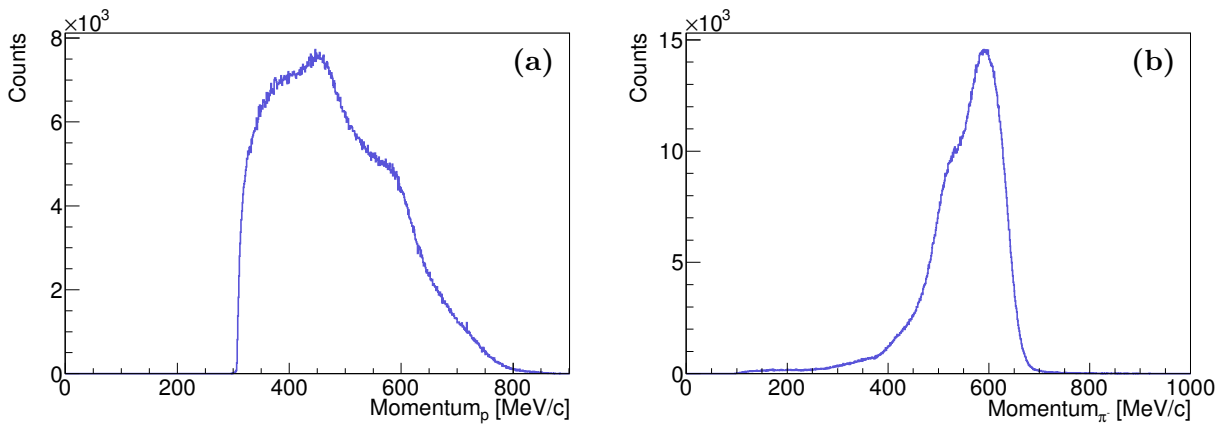
Figure 6.21: Momentum distribution of the **(a)** proton and **(b)** pion originating from elastic scattering events.

The polyethylene target is implemented in the simulation as a sensitive detector with a tube diameter of $12\,\mathrm{mm}$ and a length of $46\,\mathrm{mm}$ to be able to investigate the energy loss inside the target. Multiple scattering, ionisation, bremsstrahlung and pair production are included as physics processes for the pion and proton, respectively. The momentum distribution of the proton and pion is depicted in Fig. 6.21 (a) and (b). However, in the simulation a simplified momentum distribution was implemented. In both cases the distribution was assumed to be homogeneous ranging from $300\,\mathrm{MeV/c}$ - $800\,\mathrm{MeV/c}$ for the protons and for the pions from $400\,\mathrm{MeV/c}$ - $700\,\mathrm{MeV/c}$. The momentum is, thereby, only pointing in z-direction. Two different cases were investigated according to the emission point of the particles.

In the first case both particle species are randomly distributed along the z-axis only limited by the target length ($46\,\mathrm{mm}$) leading to a mean energy loss of $3.408\,\mathrm{MeV}$ for the protons (Fig. 6.22 (a)). Nevertheless, this value is an upper limit, since the proton originating from elastic scattering events leave the target region under an angle Θ ranging from $30° \leq \Theta \leq 70°$ (Fig. 6.15 (a)) leading to a maximal path length inside the target of $12\,\mathrm{mm}$ (Appendix A.3). The same holds for the energy loss of the pions with a mean energy loss of $0.9269\,\mathrm{MeV}$ (Fig. 6.22 (b)) having a maximal path length inside the target of $14.2\,\mathrm{mm}$ ($25° \leq \Theta \leq 80°$, Fig. 6.15 (b)). Therefore, in the second case the protons and pions are at the end of the target randomly distributed along the z-axis with a maximal path length of $12\,\mathrm{mm}$ or $14.2\,\mathrm{mm}$. This assumption is much closer to the reality, but still neglects the correct treatment of the elastic scattering kinematics according to the correct

momentum as well as the correct corrleation between the momentum and angle Θ. In this case the energy loss inside the target is much lower with a mean energy loss of $0.5722\,\text{MeV}$ (Fig. 6.22 (c)) for the protons and $0.1915\,\text{MeV}$ (Fig. 6.22 (d)) for the pions.
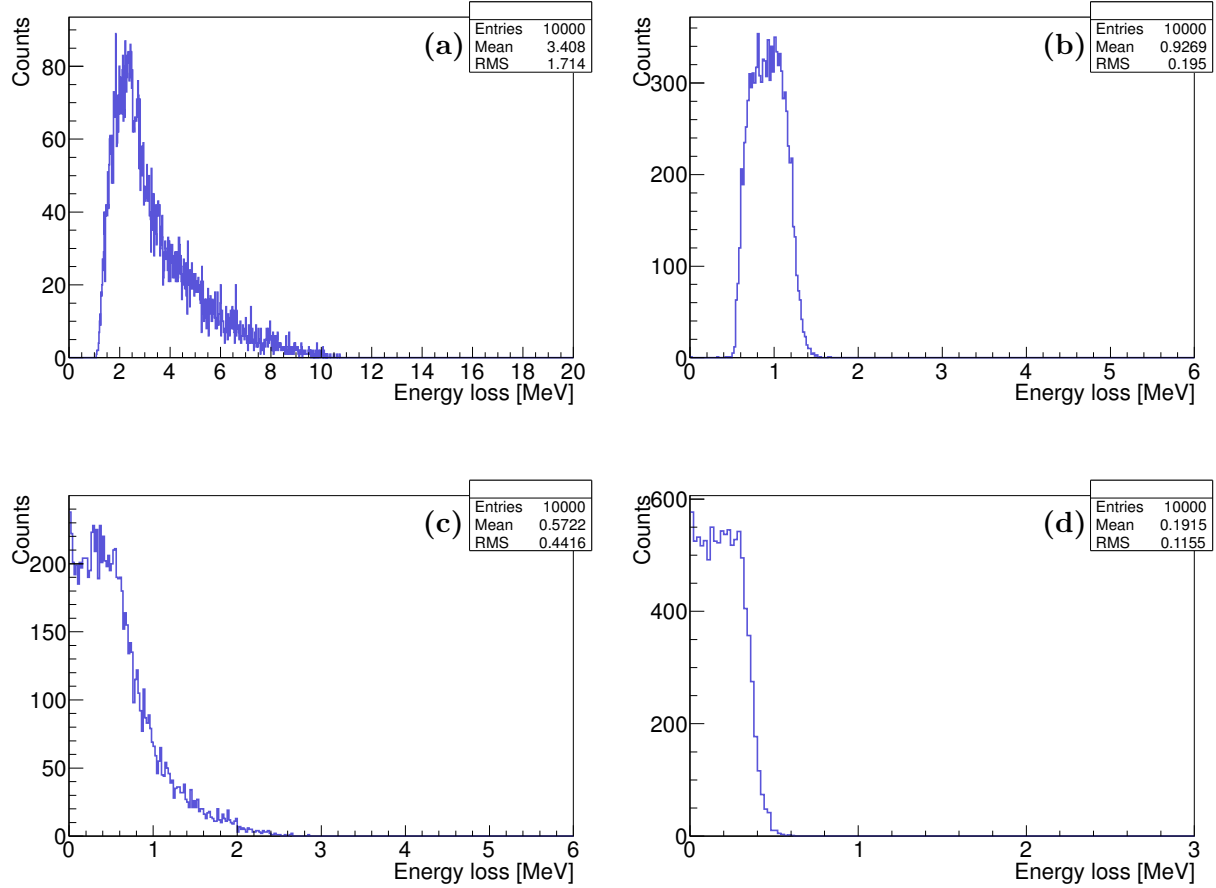
Figure 6.22: Energy loss simulation inside the polyethylene target based on GEANT4 for a flat momentum distribution (protons: $300\,\text{MeV/c}$ - $800\,\text{MeV/c}$, pions: $400\,\text{MeV/c}$ - $700\,\text{MeV/c}$) with the path length only limited by the target length **(a)** for the traversing protons and **(b)** for the traversing pions or a path length limited by the maximal path length **(c)** for the protons ($12\,\text{mm}$) and **(d)** for the pions ($14.2\,\text{mm}$).

The invariant mass spectrum of the $\pi^- p$-system can be corrected with both extracted mean energy loss values. The corrected spectra are depicted in Fig. 6.23 (a) for the first case and in Fig. 6.23(b) for the second case. For the first case the correction leads to a visible shift of the invariant mass spectrum with a new mean value of $1490\,\text{MeV}$ and therefore to a remaining difference of $\Delta(\sqrt{s_{rec}} - InvMass) = 7\,\text{MeV}$. In the second case no shift is visible with a mean value of $1488\,\text{MeV}$ ($\Delta(\sqrt{s_{rec}} - InvMass) = 9\,\text{MeV}$), since the energy loss is quite small. In both cases the energy loss inside the target is not able to explain the huge difference between the $\sqrt{s_{rec}}$ distribution calculated with the reconstructed momentum of CERBEROS and the invariant mass distribution of $9\,\text{MeV}$. Since during the simulation a lot of assumptions were taken into account, a full-scale simulation needs still to be performed including a correct treatment of the elastic scattering kinematics concerning the momentum, scattering angle and therefore path length in

the target as well as the energy loss of the pions inside the target before elastically scattering with a proton of the target.
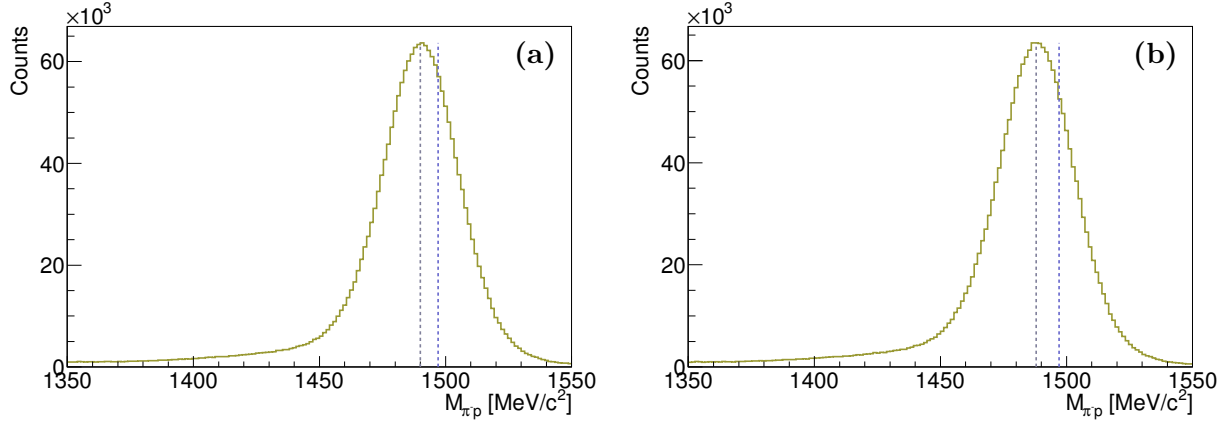
Figure 6.23: Invariant mass distribution after the correction of the mean energy loss of pions and protons inside the polyethylene target **(a)** with a mean value of 1490 MeV for a path length of the particles only limited by the target length **(b)** 1488 MeV for a maximal path length of 12 mm for the protons and for the pions of 14.2 mm. In both cases the mean value of the $\sqrt{s_{rec}}$ distribution calculated with the reconstructed pion momentum of CERBEROS is indicated with the medium blue line.

7 Summary and Outlook

Secondary pion beams have been produced with a high intensity Nitrogen beam (10^{11} part./s) impinging on a Beryllium target, correlated to a huge spread in both, momentum and position, only limited by the intrinsic beamline acceptance of around $\Delta p/p \approx 8\%$. For the later on performed exclusive analysis of investigated reactions it is necessary to measure the momentum of every pion with a resolution better than 0.5 %. Therefore, CERBEROS, a secondary beam diagnostic system, was developed to allow for on-line beam monitoring as well as the momentum reconstruction of each individual pion at high beam rates (dN/dt $> 10^6$ part./s).

The concept of CERBEROS was presented in this work and consists of two tracking stations located at different positions along the pion beam chicane. Both tracking stations are equipped with a double-sided silicon strip sensor with a large active area ($10 \times 10 \, \text{cm}^2$) covering most of the area inside the beamline. With a thickness of 300 μm and a strip pitch of 760 μm, the multiple scattering inside the sensor is kept minimal and the spatial resolution is sufficient meeting the required resolution of the pion momentum, which is reconstructed on the basis of the four extracted hit positions and the beam optics transport calculations. Each sensor is placed in a light and vacuum tight chamber (10^{-7} mbar) compatible to the beam mechanics and read out with the n-XYTER ASIC chip to guarantee fast tracking. The chip enables on-line monitoring at high rates due to its self-triggering architecture and local storage capability. The TRB3 on which the trigger logic is implemented completes the read-out chain by integrating the system into the HADES DAQ. Thereby, the HADES experiment is located at the GSI Helmholtzzentrum für Schwerionenforschung GmbH in Darmstadt and provided by the SIS18 synchrotron.

During the momentum calibration procedure with a monochromatic proton beam at six different known momenta with respect to the central beam momentum of 2.68 GeV/c the proof of concept has been provided. All reconstructed momenta are in agreement with the reference values and the resolutions are below the requirement (0.5 %) varying between 18 %-29 %.

The analysis of the data obtained during both pion-induced experimental campaigns (0.656 GeV/c − 1.7 GeV/c) is covered with special emphasis on the hit reconstruction of the x- and y-positions of each sensor as well as the momentum reconstruction based on the hit information of both tracking stations. Several selection methods for pion candidates with a certain momentum that finally interacted with the target were investigated. For the data obtained during the second experimental campaign at several central beam momenta (0.656 GeV/c - 0.800 GeV/c) a detailed study of the reconstructed momentum distribution with elastic scattering events ($\pi^- + p$) was carried out. As expected, a correlation is observed by comparing the reconstructed momentum distribution with the invariant mass spectrum of the $\pi^- p$-system reconstructed in the HADES spectrometer, since smaller momenta for the pion beam lead to smaller available energy ($\sqrt{s}$) and therefore to smaller invariant masses. However, a shift of the invariant mass spectrum to lower values compared to the $\sqrt{s}$ distribution was observed and needs further investigation. The rough estimation of the energy loss of the $\pi^- p$ pair do not explain the shift of 7 MeV yet. Therefore, a full-scale simulation of the energy loss in the target is mandatory including the kinematical constraints of elastic scattering

events as well as the broad momentum distribution of the impacting pions. Besides, a further investigation of the invariant mass spectrum is required in future including the cross-check of the magnetic field correction as well as the energy loss in the region between the target and the MDC II chambers.

Throughout both secondary pion beam runs the system demonstrated an excellent performance at high rates ($dN/dt > 10^6$ part./s) with track efficiencies and therefore reconstructed momentum efficiencies of 78.4 % at 0.690 GeV/c and even 87 % at 1.7 GeV/c.

A Momentum reconstruction

A.1 Beam optics transport code

Step number	Element
0	production target
1	in Q1
2	out Q1
3	in Q2
4	out Q2
5	in FOPI
6	FOPI
7	FOPI
8	FOPI
9	out FOPI
10	in D1
11	out D1
12	in Q3
13	out Q3
14	in Q4
15	out Q4
16	nominal interm. focus
17	detector 1
18	in Q5
19	out Q5
20	in Q6
21	out Q6
22	in D2
23	out D2
24	in Q7
25	out Q7
26	detector 2
27	in Q8
28	out Q8
29	in Q9
30	out Q9
31	interm. Point
32	HADES target
33	HADES target

A.2 Reconstructed pion momentum
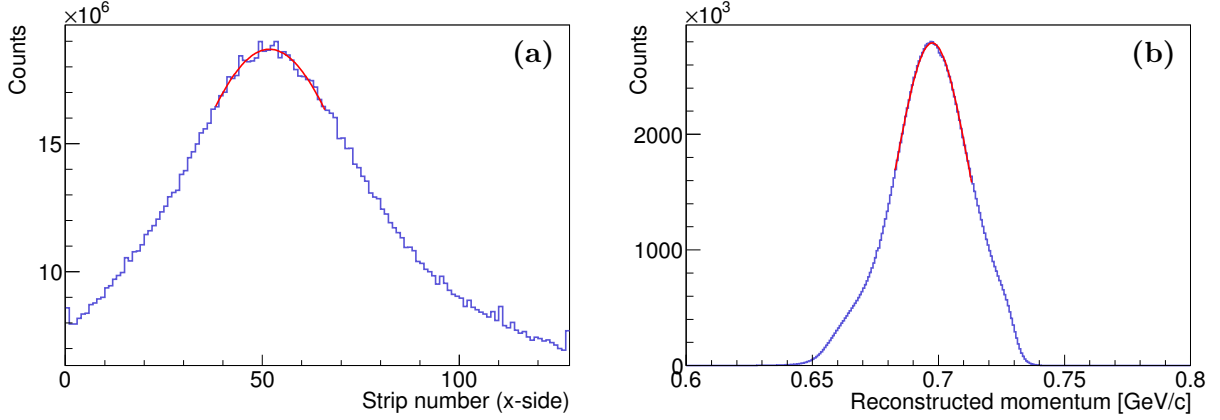
Figure A.1: **(a)** Distribution of the x-position of the first tracking station and **(b)** distribution of the reconstructed momentum for a selected data sample (*track multiplicity == 1*) collected at a central beam momentum of $0.690\,\text{GeV/c}$

In the data collected at a central beam momentum of $0.690\,\text{GeV/c}$, the beam maximum is shifted on the x-layer of the first tracking station (Fig. A.1 (a)) to lower strip numbers ($X^{det1} = 51.80$ strip number) corresponding to negative x-positions ($X^{det1} = -0.8892\,\text{cm}$) (Eq. (5.1)). Since the x-side of the first sensor is located close to the dispersive plane, the x-position is strongly coupled to the reconstructed momentum (Fig. 6.4). An estimation of the influence of a shift of the x-position (X^{det1}) on the reconstructed momentum (p_{rec}) can be done by simplifying Eq. (6.2):

$$X^{det1} \approx T_{16}^{det1} \cdot \delta, \tag{A.1}$$

where δ [%] is the momentum offset in respect to the central beam momentum $\delta = (\frac{p_{rec}-p_{ref}}{p_{ref}})$ and $T_{16}^{det1} = -0.8\,\text{cm/\%}$ [Hen14].

$$
\begin{aligned}
p_{rec} &= \delta \cdot p_{ref} + p_{ref} \\
&\approx \frac{X^{det1}}{T_{16}^{det1}} \cdot 0.690\,\text{GeV/c} + 0.690\,\text{GeV/c} \\
&\approx \frac{-0.8892\,\text{cm}}{0.8\,\text{cm/\%}} \cdot 0.690\,\text{GeV/c} + 0.690\,\text{GeV/c} \\
&\approx 0.01115 \cdot 0.690\,\text{GeV/c} + 0.690\,\text{GeV/c} \\
&\approx 0.6977\,\text{GeV/c} \\
&\approx 0.698\,\text{GeV/c}
\end{aligned}
\tag{A.2}
$$

According to the results from Eq. (A.2) the shift of beam maximum on the x-position of the first sensor is responsible for the shift of the maximum transmission of the reconstructed momentum distribution to $0.698\,\text{GeV/c}$ (Fig. A.1 (b)).

A.3 Energy loss simulation of the pion and proton in the target
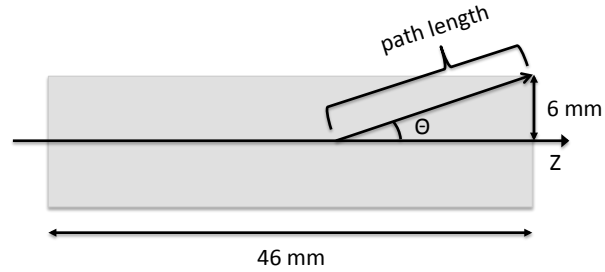
Figure A.2: Schematic of the particle trace inside the polyethylene target under an angle theta.

Calculation of the maximal *path length* of the protons ($30° \leq \varTheta \leq 70°$) and pions ($25° \leq \varTheta \leq 80°$) inside the target for the energy loss simulation.

$$path\,length = \frac{6\,\text{mm}}{\sin(\varTheta)} \tag{A.3}$$

The maximal *path length* for the protons is $12\,\text{mm}$ at $\varTheta = 30°$ and for the pions $14.2\,\text{mm}$ at $\varTheta = 25°$.

Bibliography

[Sh08]   SHKLYAR, V. AND LENSKE, H. AND MOSEL U.: *Analysis of baryon resonances in the coupled-channel Giessen model*, Springer-Verlag (2008)

[Aga09]   AGAKICHIEV, G. ET AL.: The high-acceptance dielectron spectrometer HADES. *Eur. Phys. J.* (2009), Bd. A41: S. 243–277

[Aga10]   AGAKISHIEV, G. ET AL.: In-Medium Effects on K^0 Mesons in Relativistic Heavy-Ion Collisions. *Phys. Rev.* (2010), Bd. C82: S. 044907

[Aga14a] AGAKISHIEV, G. ET AL.: Associate K^0 production in p+p collisions at 3.5 GeV: The role of $\Delta(1232)++$. *Phys. Rev.* (2014), Bd. C90: S. 015202

[Aga14b] AGAKISHIEV, G. ET AL.: Medium effects in proton-induced K^0 production at 3.5 GeV. *Phys. Rev.* (2014), Bd. C90: S. 054906

[Bar93]   BARBERIS, E. ET AL.: Temperature effects on radiation damage to silicon sensors. *Nucl. Instr. and Meth.* (1993), Bd. A326: S. 373–380

[Ben09]   BENABDERRAHMANE, M. ET AL.: Measurement of the In-Medium K^0 Inclusive Cross Section in π^--Induced Reactions at 1.15 GeV/c. *Phys. Rev. Lett.* (2009), Bd. 102: S. 182501

[Bro06]   BROGNA, A. S. ET AL.: N-XYTER, a CMOS read-out ASIC for high resolution time and amplitude measurements on high rate multi-channel counting mode neutron detectors. *Nucl. Instrum. Methods* (2006), Bd. A568: S. 301–308

[Dia02]   DIAZ, J. ET AL.: Design and commissioning of the GSI pion beam. *Nucl. Instr. and Meth.* (2002), Bd. A478: S. 511–526

[Eff99]   EFFENBERGER, M. ET AL.: e^+e^- pair production from γA reactions. *Phys. Rev.* (1999), Bd. C60: S. 044614

[Fab13]   FABBIETTI, L. ET AL.: A secondary Pion Beam for the HADES Experiment: Technical Design Report. (2013)

[Fri01]   FRIEDL, M.: *The CMS silicon strip tracker and its electronic readout*, Dissertation (2001)

[GEA]   URL `geant4.cern.ch`

[Hen14]   HENNINO, T.: Private communication (2014)

[Lal15]   LALIK, R.: Private communication (2015)

[Mak15]   MAKERT, J.: Private communication (2015)

[Man84]   MANLEY, D.M. ET AL.: Isobar-model partial-wave partial-wave analysis of $\pi N \to \pi\pi N$ in the c. m. energy range 1320-1930 MeV. *Phys. Rev.* (1984), Bd. D30: S. 904

[Mic15]   Michel, J.: Private communication (2015)

[Sch97]   Schaffner, Jurgen et al.: In-medium production of kaons at the mean field level. *Nucl. Phys.* (1997), Bd. A625: S. 325–346

[Spr08]   Spruck, B.: *Optimierung des Pionenstrahls zum HADES Detektor und Bestimmung des η-Formfaktors in Proton-Proton Reaktionen bei 2.2 GeV*, Dissertation (2008)

[Tra11]   Traxler, M. et al.: A compact system for high precision time measurements (< 14 ps RMS) and integrated data acquisition for a large number of channels. *Journal of Instrumentation* (2011), Bd. vol. 6: S. C12004

[Wei]   Weil, J. et al.: Dilepton Production in Transport-based Approches

List of Figures

List of Tables

Danksagung

Im Anschluss an meine Masterarbeit möchte ich mich bei allen bedanken, die mich in der vergangenen Zeit unterstützt haben.

Ganz besonders danke ich Prof. Laura Fabbietti, die es mir ermöglicht hat, Teil des CERBEROS-Projektes zu sein und in diesem Rahmem meine Masterarbeit zu verfassen. Sie hat mich während meiner ganzen Zeit in ihrer Gruppe gefördert und unterstützt. Insbesondere möchte ich mich bei ihr bedanken, dass sie mir schon früh ermöglichte an Konferenzen teilzunehmen. Dadurch konnte ich meine Präsentationsfähigkeit stark verbessern, sowie meinen Horizont auf neue Detektortechnologien erweitern.

Einen herzlichen Dank auch an Rafal Lalik, Ludwig Maier und Alessandro Scordo für die gute Zusammenarbeit und ihrem unermüdlichen Einsatz bei Fragen aller Art. Rafal hat mich immer bei programmier- sowie softwaretechnischen Problemen unterstützt.

Auch möchte ich Dankbarkeit der ganzen Gruppe für die sehr angenehme Arbeitsatmosphäre und die Hilfbereitschaft ausdrücken. Besonderer Dank gilt meiner Seelenverwandten und treuen Hotelzimmergenossin, Jia-Chii Berger-Chen, für ihren Beistand vor meinen Vorträgen und ihre konstruktive Korrektur meiner Masterarbeit. Zudem Danke ich Martin Berger und Robert Münzer, die mir immer mit Rat und Tat zur Seite standen. In diesem Zusammenhang auch einen großen Dank an Tobias Kunz, für die Einführung in GEANT4 und die Hilfestellung bei allen Fragen und Problemen.

Darüberhinaus auch ein herzliches Dankeschön an alle, die zwar nicht direkt bei der Konzeption und Entwicklung von CERBEROS beteiligt waren, mir jedoch hilfreich zur Seite standen. Namentlich erwähnt seien hier Ralf Lang und Michael Klöckner aus der Werkstatt, die viele Komponenten von CERBEROS angefertigt haben, wie zum Beispiel das Kühlsystem. Auch möchte ich mich bei Roman Gernhäuser bedanken, der konstruktive Ideen zum meachanischen Konzept von CERBEROS einbrachte. Für die Hilfe vor und während den Strahlzeiten danke ich der HADES-Kollaboration, inbesondere Michael Traxler, Jan Michel, Jerzy Pietraszko, Torsten Heinz und Erwin Schwab.
Mein Dank gilt auch Beatrice Ramstein und Thierry Hennino für die hilfreichen Diskussionen über die Impulsrekonstruktion.

Der größte Dank gilt meinen Eltern Karin und Uwe, meinem Bruder Jannik und meiner Oma. Sie haben mich während meines gesamten Studiums unterstützt und mir immer vermittelt, dass ich auf sie zählen kann und sie stolz auf mich sind.

Letztlich möchte ich mich noch bei Steffen Maurus und Jonas Woste für die schönen Zusammenkünfte in der Fachschaft bedanken.